

SN 2019odp – A Massive Oxygen-Rich Type Ib Supernova

T. Schweyer¹, J. Sollerman¹, A. Jerkstrand¹, M. Ergon¹, T.-W. Chen^{1,2,3}, C. M. B. Omand¹, S. Schulze⁴, M. W. Coughlin⁵, I. Andreoni⁶, C. Fremling⁷, A. Rau⁸, Y. Sharma⁷, N. L. Strotjohann⁹, L. Yan⁷, M. J. Graham⁷, M. M. Kasliwal⁷, R. R. Laher¹⁰, J. Purdum¹¹, P. Rosnet¹², B. Rusholme¹⁰, and R. Smith¹¹

¹ Department of Astronomy, The Oskar Klein Centre, Stockholm University, AlbaNova, 10691 Stockholm, Sweden, e-mail: tassilo.schweyer@astro.su.se

² Technische Universität München, TUM School of Natural Sciences, Physik-Department, James-Franck-Straße 1, 85748 Garching, Germany

³ Max-Planck-Institut für Astrophysik, Karl-Schwarzschild Straße 1, 85748 Garching, Germany

⁴ Department of Physics, The Oskar Klein Center, Stockholm University, AlbaNova, 10691 Stockholm, Sweden

⁵ School of Physics and Astronomy, University of Minnesota, Minneapolis, Minnesota 55455, USA

⁶ Department of Astronomy, University of Maryland, College Park, MD 20742, USA

⁷ Division of Physics, Mathematics and Astronomy, California Institute of Technology, Pasadena, CA 91125, USA

⁸ Max-Planck-Institut für extraterrestrische Physik, Gießenbachstraße 1, D-85748 Garching, Germany

⁹ Department of Particle Physics and Astrophysics, Weizmann Institute of Science, 234 Herzl St, 76100 Rehovot, Israel

¹⁰ IPAC, California Institute of Technology, 1200 E. California Blvd, Pasadena, CA 91125, USA

¹¹ Caltech Optical Observatories, California Institute of Technology, Pasadena, CA 91125, USA

¹² Université Clermont Auvergne, CNRS/IN2P3, LPC, F-63000 Clermont-Ferrand, France

ABSTRACT

Aims. We present and analyze observations of the Type Ib supernova (SN) 2019odp (a.k.a ZTF19abqwtfu) covering epochs within days of the explosion to the nebular phase at 360 d post-explosion. We discuss them in the context of recombination cooling emission for the early excess emission and consider progenitor models based on the nebular phase spectra.

Methods. Our observations include photometric observations mainly in the optical and low to medium-resolution spectroscopic observations covering the complete observable time-range. We expand on existing methods to derive oxygen mass estimates from nebular phase spectroscopy.

Results. Our spectroscopic observations confirm the presence of He in the SN ejecta and we thus (re)classify it as a Type Ib supernova. From the pseudo-bolometric lightcurve we estimate a high ejecta mass $M_{ej} \sim 4-7 M_{\odot}$. The high ejecta mass, large nebular [O I]/[Ca II] line flux ratio (1.2 – 1.9) and an oxygen mass above $\gtrsim 0.5 M_{\odot}$ point towards a progenitor with pre-explosion mass higher than $18 M_{\odot}$. The compact nature of the progenitor ($\lesssim 10 R_{\odot}$) suggests a Wolf-Rayet (WR) star as progenitor.

1. Introduction

Supernovae are luminous transients marking the end of the life-cycles of certain stars. The classical supernova classification scheme (Filippenko 1997) is based on the presence or absence of spectral features close to peak brightness. If hydrogen lines are present they are classified as Type II supernovae. The Type Ia sub-class is based on the presence of silicon features, while the remaining Type I supernovae fall into the Type Ib/Ic classes. Collectively the Type Ib/Ic (and Type IIb) supernovae are referred to as stripped envelope supernovae. The presence of helium further distinguish between the helium-rich Type Ib supernovae and the helium-poor Type Ic. Based on the high expansion velocities further sub-classes, such as broad-lined Type Ic (Type Ic-BL) supernovae can be distinguished. Type Ib and Ic supernovae are often considered together since they have considerable overlap in estimated explosion parameters (Lyman et al. 2016), but the actual connection to progenitor and explosion mechanism are still under debate (Modjaz et al. 2019). There also exist transitional transients, which change their type over time, motivating additional classification schemes (Prentice & Mazzali 2017; Williamson et al. 2019).

For Type Ib/Ic supernovae the progenitor stars have to lose most of their outer envelope, stripping away most of the hydrogen and/or helium. The exact mechanisms are still under debate

in the literature. One possible progenitor channel are single massive stars that eject their outer atmosphere in strong stellar winds (Puls et al. 2008; Woosley et al. 1993). One key issue here is that only the most massive stars ($M_{ZAMS} > 40 M_{\odot}$) are able to strip their hydrogen envelope completely by this mechanism. Alternatively, the evolution in a binary system could transfer the outer envelope to the companion star (Tauris et al. 2015). Direct detections of progenitors for Type Ib supernovae are still rare, with iPTF13bvn (Fremling et al. 2016) and SN 2019yvr (Kilpatrick et al. 2021) as examples. A monotonically increasing tracer for the Zero Age Main Sequence (ZAMS) mass is the oxygen mass (Laplace et al. 2021), which may be estimated using nebular phase spectra (Jerkstrand et al. 2014).

Observations shortly after first light can also yield valuable clues about shock cooling, recombination effects or nickel mixing, which can be used to constrain aspects of the outer structure of the progenitor. After a short (\sim hours) shock-breakout flash in the UV and X-ray, such as that seen in SN 2008D (Modjaz et al. 2009; Chevalier & Fransson 2008), follows the longer-lived “shock cooling envelope” (SCE) emission, which can be seen as an early excess or plateau before the main peak for stripped envelope supernovae, as discussed for Type Ib supernovae SN 2008D and SN 1999ex (Stritzinger et al. 2002). However despite more and more transients being discovered at ever earlier times thanks to large-area high-cadence survey pro-

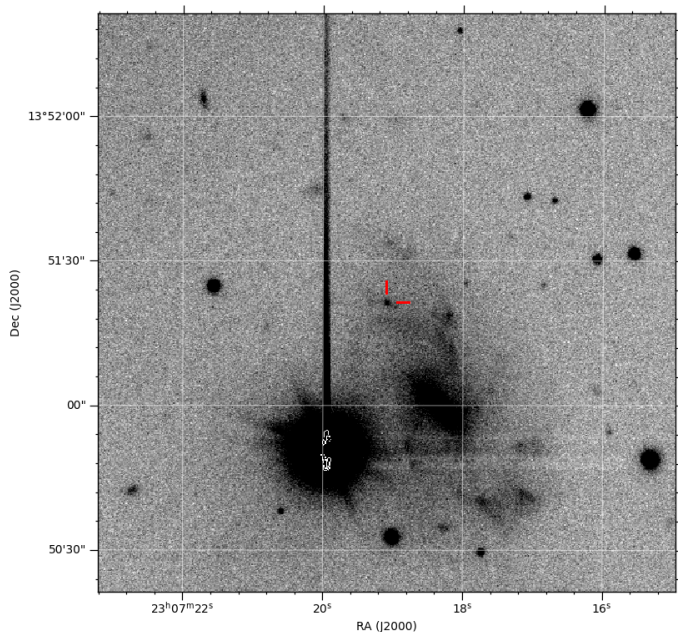


Fig. 1. Stacked r' -band GROND image using images taken between +29d and +79d showing the field of the supernova. The supernova is marked with the two red markers. The transient is located approximately 25 arcseconds from the core of the galaxy, corresponding to around 8 kpc projected separation. The bottom left of the image shows a saturated star with heavy blooming.

grammes (Bruch et al. 2021), not all supernovae show these cooling features early on, and for example iPTF13bvn showed no signs of any early excess.

In this paper we present and discuss SN 2019odp and attempt to infer some clues on the progenitor based on observations from very early to very late times. We reclassify SN 2019odp as a Type Ib supernova instead of a Type Ic-BL supernova. From the light curve we deduce a fairly large ejecta mass and a compact progenitor. The nebular spectra allow us to put a strict limits on the oxygen mass. The paper is structured as follows. In Sect. 1.1 we outline the initial discovery. In Sect. 2 we present the photometric and spectroscopic observations of the supernova, and we discuss the evolution of observables in Sect. 3. In Sect. 4 we apply (semi-)analytical models to estimate physical parameters, such as the ejecta mass, progenitor radius and the oxygen mass. Finally in Sect. 5 we discuss these properties in the context of different progenitor scenarios and summarize our findings. We use the following unless specified otherwise: the supernova phase is in observer-frame days relative to the g -band peak, all quantities are corrected for the estimated line-of-sight extinction, all magnitudes are given in the AB magnitude system, and errorbars denote 1-sigma uncertainties.

1.1. Discovery and Initial Classification

The transient SN 2019odp (ZTF19abqwtfu) was discovered as part of the Zwicky Transient Facility survey (ZTF; Bellm et al. 2019b; Graham et al. 2019) and was first reported to the Transient Name Server (TNS¹) by Nordin et al. (2019). The discovery was made on 2019 August 21 (MJD = 58716.38) in the r band with a magnitude of 18.7. The previous epoch on 2019 August 18 (MJD = 58713.44) shows a 2-sigma flux excess in the i band with a magnitude of 20.9. The last non-detection was on 2019

August 17 (MJD = 58712.48) in the g band. We define the explosion epoch t_{expl} to be at MJD 58714.5 ± 2 - the center point between the last non-detection and the first significant detection.

We estimate the g -band peak epoch, t_g^{peak} , using the interpolated g -band lightcurve (see Sect. 2.3) to be at MJD = 58734 ± 1 days. We specify the phase Δt_g^{peak} relative to this g -band peak epoch in the rest of the paper.

The transient is located at right ascension 23:07:19.090 (h:m:s) and declination +13:51:21.42 (deg:m:s; J2000.0) in the spiral galaxy UGC 12373 (see Fig. 1). Adopting the H I based redshift $z = 0.01435$ from Schneider et al. (1990) we use the derived Hubble Flow distance $D = 64 \pm 5$ Mpc and distance modulus $\mu = 34.0 \pm 0.2$ mag from NED².

On 2019 August 23 (MJD = 58718.2) SN 2019odp was classified as a Type Ic-BL supernova by Brennan et al. (2019) as part of the ePESSTO+ survey (Smartt et al. 2015). However, based on further observations we reclassify it as a Type Ib supernova in Sect. 3.7.1.

2. Observations and Data Reduction

2.1. Photometry

Follow-up photometry in the g , r and i bands were obtained using the ZTF camera (Dekany et al. 2020) mounted on the Palomar 48-inch telescope (P48) as part of the ZTF survey (Bellm et al. 2019a,b). The obtained data was processed using the ZTF pipeline (Masci et al. 2019), which detrends the images, does PSF-matching image-subtraction against stacked template images and automatic photometric calibration against field stars using the Pan-STARRS 1 (PS1; Chambers et al. 2016) survey catalog. We use ztf1c³ to perform forced photometry for all epochs. Based on this we see no outbursts before the main explosion, however we notice a small plateau before the main peak (see Fig. 3).

In addition we obtained manually triggered observations in the u , g , r and i bands using the Spectral Energy Distribution Machine (SEDM; Blagorodnova et al. 2018) Rainbow Camera mounted on the Palomar 60 inch telescope (P60). The obtained data was automatically processed using the SEDM-RC pipeline (Fremling et al. 2016).

We also obtained some post-peak follow-up photometry in the $g'r'i'z'JHK_s$ bands using the Gamma-ray Burst Optical/Near-infrared Detector (GROND; Greiner et al. 2008) mounted on the MPG 2.2m telescope located at the ESO La Silla observatory. The data is reduced using a *pyraf/IRAF*-based⁴ pipeline (Krühler et al. 2008). For the near-infrared (NIR) bands, aperture photometry was performed. The $g'r'i'z'$ bands are calibrated against the Sloan Digital Sky Survey Data Release 15 catalog (SDSS DR15; Aguado et al. 2019) and the NIR JHK_s bands are calibrated against the Two Micron All Sky Survey catalog (2MASS; Skrutskie et al. 2006). The GROND NIR Vega magnitudes are converted to AB magnitudes using Blanton & Roweis (2007).

Late time optical photometry in the g , r and i bands were obtained using the Alhambra Faint Object Spectrograph and

² Which adopts the following cosmology parameters: $H_0 = 67.8$ km s⁻¹ Mpc⁻¹, $\Omega_{\text{matter}} = 0.308$ and $\Omega_{\text{vacuum}} = 0.692$. We use the value for the peculiar velocities that include the Virgo, great attractor and Shapley supercluster velocities fields from NED (Mould et al. 2000).

³ <https://github.com/MickaelRigault/ztf1c> by M. Rigault

⁴ Science Software Branch at STScI (2012); National Optical Astronomy Observatories (1999)

¹ <https://www.wis-tns.org/>

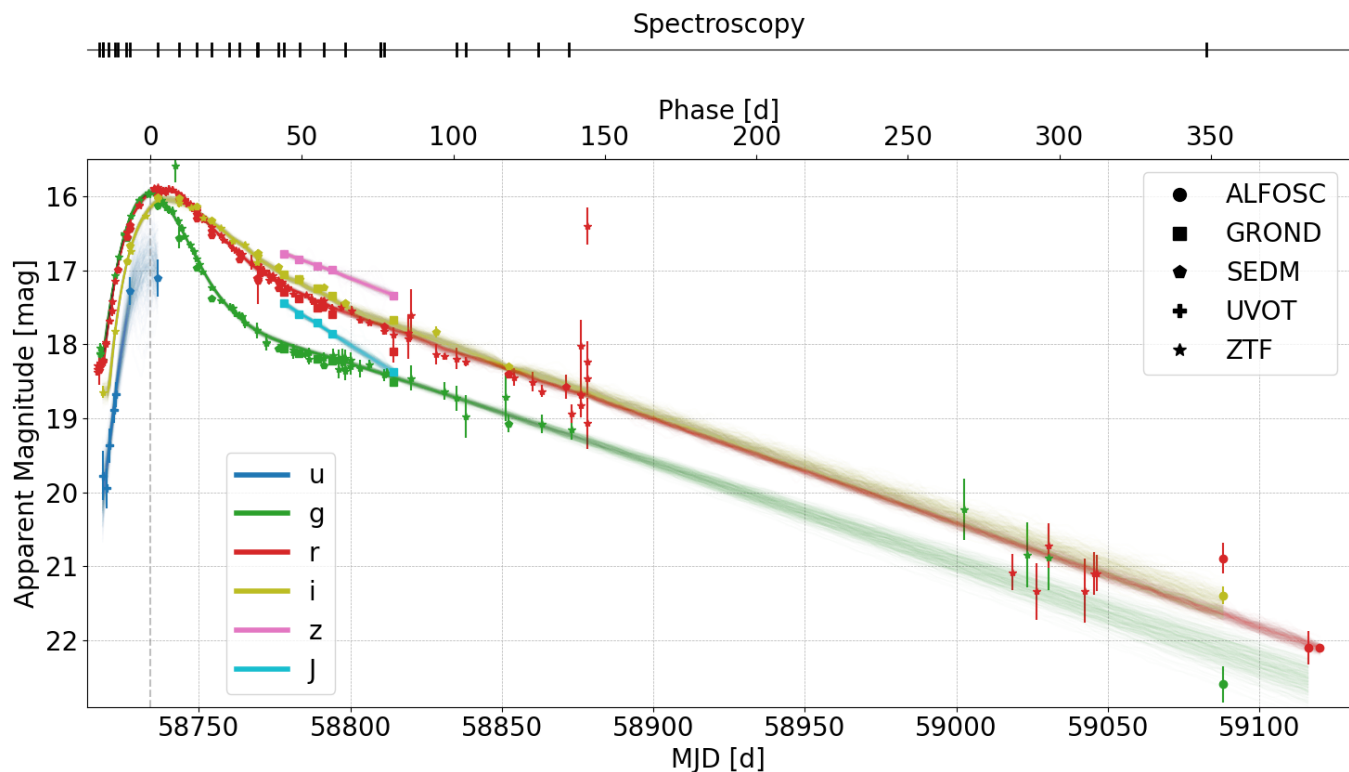


Fig. 2. Photometric evolution of SN 2019odp in the *ugrizJ* bands using the combined photometry dataset. The color denotes the band and the different markers denote the source instrument. The interpolation lightcurves (as used for constructing the color evolution and bolometric lightcurves) are faintly overlaid (see Sect. 2.3 for a detailed description). The lightcurve is not corrected for extinction. The times of spectroscopic observations are marked in the top bar by vertical lines.

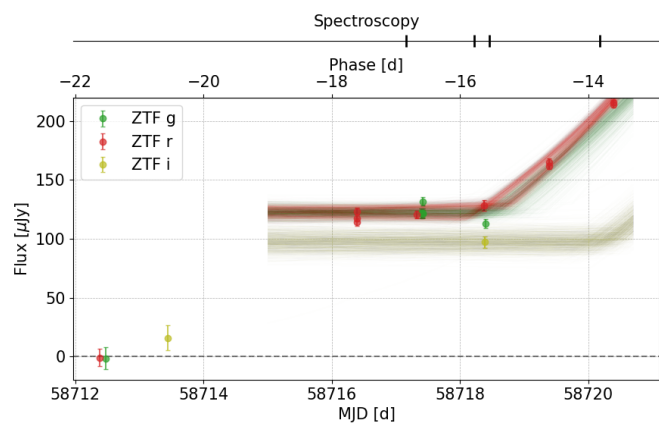


Fig. 3. Photometric evolution of SN 2019odp around the discovery epoch. The lightcurve is given in flux units to easily show the pre-discovery upper limits on the same scale. The different colors denote the different bands. The zero flux level is denoted by a dashed line. The lightcurve is not corrected for extinction. The times of spectroscopic observations are marked in the top bar by vertical lines.

Camera instrument (ALFOSC) mounted on the Nordic Optical Telescope (NOT). The observations are reduced using the *PyNOT*⁵ pipeline. We then perform image subtraction using *hot-*

⁵ <https://github.com/jkrogager/PyNOT> by Jens-Kristian Krogager.

pants (Becker 2015) against matching PS1 images as a template. Resampling of the template image to the same pixel scale as the science images is performed using *SWarp* (Bertin et al. 2002). Aperture photometry is then performed on the difference image using *photutils* (Bradley et al. 2021).

To extend the wavelength coverage to the ultra-violet (UV), we utilised the 30 cm UV Optical Telescope (UVOT; Roming et al. 2005) onboard the Neil Gehrels Swift Observatory (Gehrels et al. 2004). We retrieved science-ready data from the Swift archive⁶. We first co-added all sky exposures for a given epoch and filter using *uvotimsum* in HEASoft⁷ version 6.26.1. Afterwards, we measured the brightness of SN 2019odp with the Swift tool *uvotsource*. The source aperture had a radius of 3'' while the background region had a significantly larger radius. The photometry was calibrated with the latest calibration files from September 2020 and converted to the AB system using Breeveld et al. (2011).

The combined lightcurve is shown in Fig. 2 and a list of photometric measurements is provided in Table 1. For the first 70 days the lightcurve has an average cadence of 2 days in the *g* band (no gap larger than 4 days), 1 day in *r* band (no gap larger than 5 days) and 3 days in *i* band (no gap larger than 7 days).

2.2. Spectroscopy

The first spectrum was obtained on 2019 August 21 - less than a day after the discovery - using the SEDM Integral Field Unit

⁶ https://www.swift.ac.uk/swift_portal

⁷ <https://heasarc.gsfc.nasa.gov/docs/software/heasoft/>

UT	MJD (d)	Δt_{expl} (d)	Δt_g (d)	Filter	Telescope/Instrument	m (mag)	Δm (mag)	m_{lim} (mag)	F (μJy)	ΔF (μJy)
2019-08-17 09:01	58712.4	-2.1	-21.6	r	P48/ZTF	nan	nan	20.11	-1.0	7.4
2019-08-17 11:26	58712.5	-2.0	-21.5	g	P48/ZTF	nan	nan	19.89	-1.5	9.3
2019-08-18 10:28	58713.4	-1.1	-20.6	i	P48/ZTF	20.91	0.76	19.83	15.7	10.6
2019-08-21 09:19	58716.4	1.9	-17.6	r	P48/ZTF	18.72	0.05	21.26	117.7	3.1
2019-08-21 09:23	58716.4	1.9	-17.6	r	P48/ZTF	18.76	0.05	21.21	114.2	3.2
2019-08-21 09:24	58716.4	1.9	-17.6	r	P48/ZTF	18.67	0.05	21.23	123.4	3.1
2019-08-22 07:52	58717.3	2.8	-16.7	r	P48/ZTF	18.70	0.05	21.12	120.6	3.1
2019-08-22 09:28	58717.4	2.9	-16.6	g	P48/ZTF	18.69	0.07	20.95	121.8	4.2
2019-08-22 09:52	58717.4	2.9	-16.6	g	P48/ZTF	18.69	0.07	21.04	121.7	3.8
2019-08-22 09:53	58717.4	2.9	-16.6	g	P48/ZTF	18.69	0.07	21.13	120.9	3.6
2019-08-22 09:53	58717.4	2.9	-16.6	g	P48/ZTF	18.60	0.06	21.16	131.7	3.3
2019-08-23 04:07	58718.2	3.7	-15.8	UVW1	Swift/UVOT	21.17	0.35	21.24	12.4	4.0
2019-08-23 04:09	58718.2	3.7	-15.8	U	Swift/UVOT	20.49	0.34	20.62	23.1	7.1
2019-08-23 04:10	58718.2	3.7	-15.8	B	Swift/UVOT	18.91	0.18	19.91	99.1	16.7
2019-08-23 04:13	58718.2	3.7	-15.8	UVW2	Swift/UVOT	22.81	0.59	22.05	2.7	1.5
2019-08-23 04:17	58718.2	3.7	-15.8	V	Swift/UVOT	18.59	0.28	18.98	133.0	34.0
2019-08-23 04:28	58718.2	3.7	-15.8	UVM2	Swift/UVOT	22.41	0.29	22.79	3.9	1.0
2019-08-23 08:55	58718.4	3.9	-15.6	r	P48/ZTF	18.63	0.07	20.62	128.1	4.6
2019-08-23 09:19	58718.4	3.9	-15.6	i	P48/ZTF	18.93	0.08	20.72	97.3	4.9
2019-08-23 09:35	58718.4	3.9	-15.6	g	P48/ZTF	18.77	0.07	21.01	112.8	3.8
2019-08-24 09:10	58719.4	4.9	-14.6	r	P48/ZTF	18.35	0.04	21.34	165.3	2.7

Table 1. Listing of the full forced photometry dataset obtained for SN 2019odp. ZTF photometry is based on image subtraction forced photometry and contains pre-explosion epochs. Both magnitudes as well as fluxes are given. No foreground/host extinction correction nor any other secondary correction steps are applied. The full photometry table are available on Zenodo at <https://zenodo.org/record/7554926> (which also contains a second file with all corrections applied.)

UT	MJD (d)	Δt_{expl} (d)	Δt_g (d)	Telescope/Instrument	Setup	Airmass	Exp. Time (s)
2019-08-22 03:52	58717.2	2.7	-16.8	P60/SED	IFU	3.0	2250
2019-08-23 05:23	58718.2	3.7	-15.8	ESO-NTT/EFOSC	1.0-slit/Gr13	1.4	900
2019-08-23 10:55	58718.5	4.0	-15.5	P60/SED	IFU	1.2	2250
2019-08-25 04:15	58720.2	5.7	-13.8	P60/SED	IFU	2.2	2250
2019-08-27 08:44	58722.4	7.9	-11.6	P200/DBSP	600/4000	1.1	300
2019-08-28 04:06	58723.2	8.7	-10.8	P60/SED	IFU	2.2	2250
2019-08-30 23:35	58726.0	11.5	-8.0	NOT/ALFOSC	Gr4	1.2	1200
2019-09-01 04:56	58727.2	12.7	-6.8	P60/SED	IFU	1.5	1800
2019-09-10 07:19	58736.3	21.8	2.3	P60/SED	IFU	1.1	1800
2019-09-17 07:44	58743.3	28.8	9.3	P60/SED	IFU	1.1	1800
2019-09-23 02:48	58749.1	34.6	15.1	P60/SED	IFU	1.9	1800
2019-09-28 05:56	58754.2	39.7	20.2	P60/SED	IFU	1.1	1800
2019-10-03 22:20	58759.9	45.4	25.9	NOT/ALFOSC	Gr4	1.1	1800
2019-10-07 05:35	58763.2	48.7	29.2	P60/SED	IFU	1.1	1800
2019-10-13 07:06	58769.3	54.8	35.3	P60/SED	IFU	1.1	1800
2019-10-13 07:47	58769.3	54.8	35.3	P60/SED	IFU	1.3	1800
2019-10-20 05:46	58776.2	61.7	42.2	P60/SED	IFU	1.1	2250
2019-10-22 00:46	58778.0	63.5	44.0	NOT/ALFOSC	Gr4	1.3	2200
2019-10-27 03:34	58783.1	68.6	49.1	P60/SED	IFU	1.1	2250
2019-11-04 02:02	58791.1	76.6	57.1	P60/SED	IFU	1.2	2250
2019-11-11 03:33	58798.1	83.6	64.1	P60/SED	IFU	1.1	2250
2019-11-22 22:20	58809.9	95.4	75.9	NOT/ALFOSC	Gr4	1.2	2200
2019-11-24 06:12	58811.3	96.8	77.3	P60/SED	IFU	1.6	2250
2019-12-18 02:26	58835.1	120.6	101.1	P60/SED	IFU	1.1	2250
2019-12-21 03:58	58838.2	123.7	104.2	P60/SED	IFU	1.4	2250
2020-01-04 03:21	58852.1	137.6	118.1	P60/SED	IFU	1.5	2250
2020-01-13 20:27	58861.9	147.4	127.9	NOT/ALFOSC	Gr4	1.6	2700
2020-01-24 05:30	58872.2	157.7	138.2	Keck-I/LRIS	1.0-slit/400/3400/8500	2.0	300
2020-08-21 11:58	59082.5	368.0	348.5	Keck-I/LRIS	1.0-slit/400/3400/8500	1.0	1363

Table 2. Observation log of the spectroscopic observations.

(SEDM IFU; Blagorodnova et al. 2018). The observations were reduced using the *pysedm* package (Rigault et al. 2019).

We obtained further followup spectroscopy using the SEDM and the NOT ALFOSC spectrograph. In addition we obtained one pre-peak spectrum using the Double Spectrograph (DBSP; Oke & Gunn 1982) mounted on the Palomar 200 inch telescope (P200). In total we obtained 8 spectra before peak, and 30 spectra in total. This also includes the public NTT classification spectrum from Brennan et al. (2019) under the ePESSTO programme.

We also obtained two high signal-to-noise (S/N) late-time spectra using the Low Resolution Imaging Spectrograph (LRIS; Oke et al. 1995) mounted on the Keck 1 telescope. The LRIS observations were reduced using the fully automated pipeline by Perley (2019).

All spectra are absolute flux-calibrated using synthetic r -band photometry, derived using the *speclite*⁸ package, against the interpolated lightcurve dataset (see Sect. 2.3).

We show the spectral sequence split into early phase (Fig. 10), photospheric phase (Fig. 11), pre-nebular phase (Fig. 12) and nebular phase (Fig. 13). The full log of spectroscopic observations can be found in Table 2. The observation epochs are also indicated in the upper part of the light curve figure (Fig. 2). The final reduced and flux-calibrated spectra are available on WISEREP⁹ (Yaron & Gal-Yam 2012).

2.3. Lightcurve Interpolation and Parameter Estimation

For SN 2019odp and the comparison sample (see Sect. 3.2) we perform lightcurve dataset combination, interpolation and fitting using the same framework. First we pre-process the individual instrument lightcurves by transforming all photometry to the AB system and correcting for the extinction with instrument-specific coefficients (see Sect. 3.1 for SN 2019odp and Sect. 3.2 for the used values for the comparison sample). We use Gaussian Process interpolation (see Görtler et al. (2019) for a review) to produce per-band lightcurves combining the different photometric datasets from the different instruments. Simultaneously we estimate empirical lightcurve observables, such as late-time decline rate and peak time, by fitting empirical model functions to the lightcurves. This is done by using them as the mean function in the Gaussian Process. These photometric model functions are described in Appendix A.

We use the *dynesty* dynamic nested sampler (Speagle 2020; Skilling 2004, 2006; Higson et al. 2019) to estimate the posterior distribution of the model parameters as well as the amplitude and length-scale parameters of the Gaussian Process Matern-3/2 kernel. When more than one photometric instrument (with a nominally similar photometric filter system) and overlapping observations are available we also include an offset parameter in the parameter estimation. The offsets are stated relative to the photometric instrument with the best coverage (for instance ZTF in the case of SN 2019odp).

3. Analysis

3.1. Extinction

Based on the dust maps by Schlafly & Finkbeiner (2011) we can estimate the Milky way extinction $E(B - V)$ at the position of the transient to be in the range from 0.14 to 0.20 mag. For analysis requiring extinction-corrected values we propagate the uncertainty using Monte Carlo methods. We assume no host extinction based on the lack of any visible sodium absorption features. In addition, we compare the colors against the intrinsic color templates at +10 d from Stritzinger et al. (2018) and notice that our supernova has bluer $g-r$ and $g-i$ colors than any supernova class in that study. Comparing our lightcurve against the lightcurves of the sample supernovae that the Stritzinger color templates are based on, we notice that SN 2019odp is bluer at virtually any time. This further strengthens our assumption of no host galaxy extinction for this event.

We use the computed $A_x/E(B - V)$ values for the different filters from Schlafly & Finkbeiner (2011) for $R_V = 3.1$ for all photometric extinction corrections. We use the *extinction* (Barbary 2016) python implementation of the Cardelli et al. (1989) extinction law to extinction correct all spectra.

3.2. Comparison Datasets

We compare the properties of SN 2019odp against a selected sample of well-observed objects from the literature that are prototypes for the different supernova classes: SN 1998bw (Ic-BL) and SN iPTF13bvn (Ib). We also include SN 2002ap (Ic-BL) since it has the same peak-brightness and might be a more suitable comparison objects for Type Ic-BL supernovae than the much brighter SN 1998bw. We also include SN 2008D (Ib) since it was a very close match spectroscopically and showed somewhat similar unusual behaviour right after discovery. The adopted supernova parameters for the comparison objects are presented in Table 3.

For SN 1998bw we use the *UBVRI* lightcurves compiled by Clocchiatti et al. (2011). For iPTF13bvn we use the *gri* lightcurve by Fremling et al. (2016) with additional *U*-band UVOT photometry points from Brown et al. (2014). For SN 2008D we use the *BVg'r'* lightcurves from Bianco et al. (2014) and the UVOT *U*-band lightcurve from Brown et al. (2014). For SN 2002ap we use the *UBVRI* lightcurves compiled by Foley et al. (2003). Where necessary we convert the magnitudes from Vega to AB magnitudes and we use the same interpolation procedure as described in Sect. 2.3.

3.3. Photometric Evolution

In this section, we compare the photometric evolution of SN 2019odp with our previously defined comparison transients. A light-curve comparison is shown in Fig. 4. We estimate most lightcurve observables using the method described in Sect. 2.3 applied to a Contardo et al. (2000) model modified to include an early plateau phase (see Appendix A). The remaining observables are estimated using a Monte Carlo sampling technique. All derived observables for each transient and photometric band are presented in Table 4.

Zooming in on the time-period around discovery (see Fig. 3) shows that the initial lightcurve evolution for SN 2019odp is more consistent with a plateau than with an exponential rise. This behaviour is seen in both the g and r band (i -band data has too low cadence). Comparing the r - and g -band lightcurves be-

⁸ <https://github.com/desihub/speclite>

⁹ <https://wiserep.weizmann.ac.il/>

Supernova	Type	t_{expl} (d)	t_{peak} (d)	Distance (Mpc)	$E(B - V)_{\text{MW}}$ (mag)	$E(B - V)_{\text{Host}}$ (mag)	Phot. Velocity v_{ph} (km s ⁻¹)
SN 1998bw	Ic-BL	50928.909 (8)	50945 ± 3	40.84 ± 2.86 (0)	0.047 – 0.06 (1)	0 (5)	19500 ⁺¹⁷⁰⁰ ₋₁₀₀₀ (3)
SN 2002ap	Ic-BL	52300 ± 0.5 (9)	52313 ± 3	10.69 ± 0.75 (0)	0.0585 – 0.0661 (1)	0.01 – 0.02 (6)	13000 ⁺²⁰⁰⁰ ₋₁₀₀₀ (3)
SN 2008D	Ib-pec	54474.564 (7)	54493 ± 3	33.69 ± 2.36 (0)	0.0193 ± 0.0002 (1)	0.4 – 0.8 (4)	9500 ⁺²¹⁰⁰ ₋₁₀₀₀ (3)
iPTF13bvn	Ib	56458.7 ± 0.1 (2)	56477 ± 3	26.8 ± 2.6 (2)	0.0421 – 0.0448 (1)	0.04 – 0.15 (2)	8000 ± 1000 (3)

Table 3. Adopted parameters for the comparison objects. The photospheric velocity is the estimated velocity at the lightcurve peak. In case a range is specified a uniform prior is used, in the other case a (asymmetric) gaussian is used as prior. The source for each parameter has been denoted in parantheses. References: (0) NED; (1) IRSA DUST Service using Schlafly & Finkbeiner (2011) map; (2) Fremling et al. (2016); (3) Lyman et al. (2016); (4) Soderberg et al. (2008); (5) Clocchiatti et al. (2011); (6) Takada-Hidai et al. (2002); (7) Modjaz et al. (2009); (8) Soffitta et al. (1998); (9) Mazzali et al. (2002).

tween SN 2019odp and SN 2008D, which is another supernova that showed signs of an early plateau or a shock cooling peak, the bump appears at roughly the same relative phase (possibly slightly earlier in SN 2019odp) and is fainter in SN 2019odp than in SN 2008D. The bump is ~ 1 mag fainter in r band, ~ 2 mag fainter in i band and ~ 3 mag fainter in the g band. We estimate the absolute plateau magnitude for SN 2019odp to be $-14.48^{+0.24}_{-0.21}$ mag in g band, $-14.23^{+0.20}_{-0.19}$ mag in r band and $-13.69^{+0.28}_{-0.28}$ mag in the i band.

Following the plateau, SN 2019odp rises to the main peak in 14–15 days in g band, 17–21 days in r band and 17–21 days in i band (measured as time between the first data point $\geq 3\sigma$ above the plateau level and peak). The Contardo rise-time parameter is ~ 8 days (see Table 4). The light curve for SN 2019odp peaks at an absolute magnitude of ~ -18 in the gri bands (see Table 4 for the exact values for each band). This is towards the brighter end of the luminosity distribution previously established for Type Ib supernovae (Taddia et al. 2015), but within the bulk of the distribution for Type Ic-BL supernovae (Taddia et al. 2019). In the r band, the supernova shows a rather flat peak at an apparent magnitude of 15.9 that is at least 7 days in duration. No plateau can be seen in the g or the i bands (limited by the sampling period at peak). The main peak is several days wider in all bands compared to the lightcurves of iPTF13bvn and SN 2008D and more closely resembles the width of SN 1998bw. This difference is most pronounced in the r and i bands. The peak width σ of the fitted Gaussian is given in Table 4.

The Contardo late-time decline parameter in all bands is significantly slower for SN 2019odp than for the comparison objects. The measured linear slopes are provided in Table 4.

3.4. Color Evolution

During the very early ≥ 2 -day plateau-phase both the $g-r$ colors (shown in the upper panel of Fig. 5) and the $r-i$ colors (shown in Fig. 5, lower panel) are more blue than for any of the comparison objects. The $g-r$ color stays constant during this phase showing no bump unlike all comparison objects. Afterwards the $g-r$ color of SN 2019odp evolves to a more red color, but this evolution happens later and is slower than in the comparison objects. It gets redder until it meets the color lightcurve of iPTF13bvn at around 25 days post-peak and afterwards follows the same evolution. The $r-i$ color shows an early time valley around 10 days before peak, which is unseen or much weaker in the comparison objects before becoming redder again and joining the evolution of the other supernovae (which mostly stay constant after 40 days post-peak).

The initial $U-r$ color evolution of SN 2019odp matches that of iPTF13bvn. However at around -5 days for iPTF13bvn,

the $U-r$ color quickly starts to get redder, while SN 2019odp only starts getting redder after the peak. Due to the limited U -band observations the exact inflection point is not known. One interesting observation is that while SN 2019odp has bluer colors in all other color indices this is not true in the $U-r$ color, where SN 2008D starts almost 1 magnitude bluer and monotonically gets redder.

3.5. Blackbody Evolution

We estimate blackbody parameters using the interpolated photometry datasets for all supernovae in the comparison sample (Sect. 2.3). We use the gri bands when available and the closest matches in wavelength if not. The detailed description and validation of the method can be found in Appendix C. The time-evolution of the photospheric temperature and radius is shown in Fig. 6.

Initially SN 2019odp is both hotter and the initial photospheric radius is smaller than for any of the comparison objects. This is most likely an under-estimate of the true photospheric temperature (and at the same time a slight over-estimate of the radius), since the blue part of the spectral energy distribution (SED) seems to be suppressed (only considering the ri bands yields a closer match to the full $grizJH$ photometry modelling for the time-period post-peak when it is available). Roughly 20 days after peak the temperature evolution for SN 2019odp joins that of most other supernovae in the comparison sample. SN 2019odp shows a larger peak photospheric radius compared to all comparison transients except SN 1998bw.

3.6. Pseudobolometric Light Curve

Using the photometric datasets (Sect. 2.3) for SN 2019odp and the comparison sample we compute pseudobolometric lightcurves with the Lyman et al. (2014) method using the g and r band (or closely corresponding bands for some of the comparison transients). The derived pseudobolometric light curves are shown in the right panel of Fig. 4. We first estimate the peak epoch of the pseudobolometric lightcurve by sampling the interpolated lightcurve (excluding any uncertainties that affect the lightcurve globally) in a 10 day window around the g -band peak epoch and then selecting the time of the brightest point for each sampled lightcurve. We estimate the peak magnitude by sampling the interpolated lightcurve at the peak epoch (including global uncertainties), which yields:

$$M_{\text{pbol,peak}} = -17.9^{+0.20}_{-0.21} \text{ mag.} \quad (1)$$

We convert the absolute pseudobolometric magnitudes to luminosities using the bolometric luminosity of the Sun $L_{\text{bol},\odot} =$

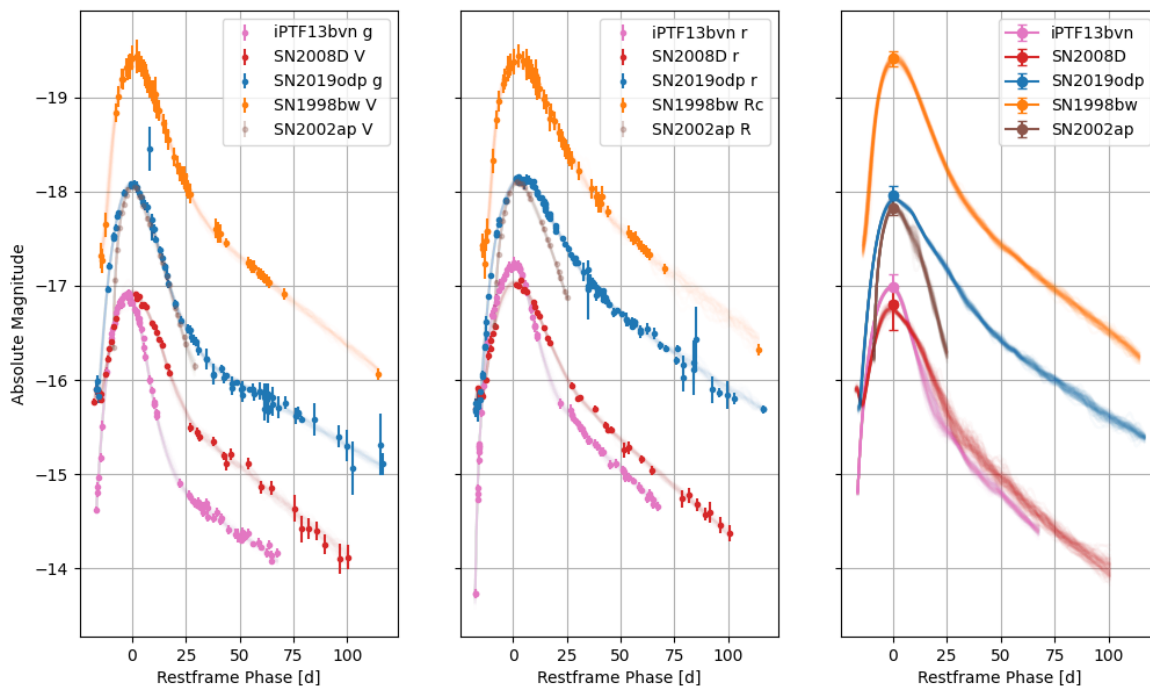


Fig. 4. Comparison of the evolution of the absolute lightcurves in g (left panel) and r (middle panel) bands between SN 2019odp and selected comparison objects. In addition the quasi-bolometric lightcurve derived using the Lyman method is shown (right panel). In the pseudobolometric lightcurve, the error bars around the peak represent the combined error from the distance uncertainty, extinction uncertainty and the scatter from the Lyman relation. The interpolated light curves for each supernova are overlaid the observed datapoints in the same color. These are used to derive the pseudobolometric lightcurves in the right panel.

$3.828 \times 10^{33} \text{ erg s}^{-1}$, and $M_{bol,\odot} = 4.74 \text{ mag}$, to get:

$$L_{\text{pbol,peak}} = 44_{-7}^{+10} \times 10^{41} \text{ erg s}^{-1}. \quad (2)$$

This is well in line with peak pseudobolometric luminosities seen previously for Type Ib supernovae (Lyman et al. 2016) or Type Ic-BL supernovae (Taddia et al. 2019). As one would expect based on the photometric comparison (see Sect. 3.3) the pseudobolometric main peak is also wider than for most of the comparison objects (see right panel in Fig. 4). The time-integrated total radiated luminosity is:

$$L_{\text{pbol,int}} = 2.1_{-0.4}^{+0.4} \times 10^{49} \text{ erg}. \quad (3)$$

We also measure the duration of the early plateau to be in the range of 2 to 5 days. Using direct integration of the photometric measurements in the ZTF gri bands we estimate the plateau pseudobolometric luminosity to be:

$$L_{\text{pbol,plat}} = 2.1_{-0.4}^{+0.4} \times 10^{41} \text{ erg s}^{-1}, \quad (4)$$

which corresponds to $M_{\text{pbol,plat}} \approx -14.6 \text{ mag}$.

3.7. Spectroscopic Evolution

We present the early spectral evolution between discovery and peak in Fig. 10. The first spectrum, taken 16.8 days before peak, is mostly blue and featureless with some suppression of the blue side of the spectrum. The second spectrum, taken one day later, is dominated by a staircase-shaped continuum that has flat regions in the ranges $5570 - 6670 \text{ \AA}$ and $7050 - 9000 \text{ \AA}$ with some narrow emission lines that we identify as host galaxy contamination. While the first spectrum of the sequence could still be explained by a single (partially absorbed) blackbody the later spectra clearly show signs of emission or absorption lines.

The first identifiable line features are seen in the spectrum at a phase of -12 days. We can identify two P-Cygni features that we associate with $\text{He I } \lambda\lambda 5876, 6678$ and possibly $\text{He I } \lambda 4471$ at roughly 14000 km s^{-1} and with blue-shifted emission peaks. We investigate the velocity evolution of the helium feature in more detail in Sect. 3.7.2.

After peak the lines gain in strength, the helium P-Cygni features become much more pronounced and additional lines such as the various forbidden calcium lines become visible. The spectral evolution in the photospheric phase is shown in Fig. 11. A feature that is possibly associated with $\text{Mg I } \lambda 4571$ becomes more obvious. At around 5000 \AA a feature becomes visible which could be $[\text{O III}] \lambda\lambda 4959, 5007$. This line was first identified by Lunnan et al. (2016) in super-luminous supernovae (SLSN) and is seen in SLSN model spectra by Jerkstrand et al. (2017). We can identify similar features in the comparison Type Ib supernovae SN 2008D and iPTF13bvn, which suggests that this

Supernova	Band	Δm_{-10} (mag)	Δm_{15} (mag)	Linear Slope (mmag/d)	M_{\max} (mag)	Peak Width (d)	Rise Timescale (d)
SN 2019odp	g	$0.81^{+0.01}_{-0.01}$	$0.85^{+0.01}_{-0.01}$	$13.5^{+0.3}_{-0.3}$	$-18.08^{+0.08}_{-0.10}$	$16.1^{+0.6}_{-0.8}$	$13.1^{+1.9}_{-2.6}$
SN 1998bw	V	$0.84^{+0.08}_{-0.06}$	$0.72^{+0.03}_{-0.03}$	$18.6^{+0.1}_{-0.1}$	$-19.37^{+0.08}_{-0.08}$	$16.6^{+0.4}_{-0.5}$	$7.1^{+1.7}_{-1.9}$
SN 2002ap	V	< 3.5	$0.90^{+0.03}_{-0.03}$	$19.2^{+0.2}_{-0.2}$	$-18.05^{+0.07}_{-0.06}$	$15.5^{+0.6}_{-0.8}$	$1.7^{+0.3}_{-0.2}$
SN 2008D	V	$0.53^{+0.02}_{-0.02}$	$0.67^{+0.02}_{-0.02}$	$19.1^{+0.6}_{-0.7}$	$-16.93^{+0.17}_{-0.13}$	$14.1^{+0.7}_{-0.7}$	< 16.4
iPTF13bvn	g	$1.15^{+0.03}_{-0.03}$	$1.34^{+0.02}_{-0.02}$	$19.7^{+0.2}_{-0.2}$	$-16.89^{+0.11}_{-0.11}$	$11.0^{+0.2}_{-0.2}$	$4.7^{+1.0}_{-0.7}$
SN 2019odp	r	$0.42^{+0.02}_{-0.02}$	$0.44^{+0.01}_{-0.01}$	$14.1^{+0.1}_{-0.1}$	$-18.13^{+0.10}_{-0.09}$	$21.2^{+0.4}_{-0.6}$	$10.0^{+0.7}_{-0.6}$
SN 1998bw	Rc	$0.72^{+0.07}_{-0.07}$	$0.49^{+0.03}_{-0.03}$	$16.3^{+0.1}_{-0.1}$	$-19.37^{+0.08}_{-0.07}$	$22.6^{+1.0}_{-1.0}$	$5.9^{+1.4}_{-1.3}$
SN 2002ap	R	$0.96^{+0.05}_{-0.06}$	$0.70^{+0.01}_{-0.01}$	$15.7^{+0.2}_{-0.1}$	$-18.10^{+0.08}_{-0.07}$	$16.9^{+0.7}_{-0.8}$	$2.8^{+1.4}_{-0.4}$
SN 2008D	r	$0.50^{+0.02}_{-0.02}$	$0.56^{+0.01}_{-0.01}$	$19.8^{+0.4}_{-0.4}$	$-17.02^{+0.15}_{-0.14}$	$15.4^{+0.7}_{-0.8}$	$9.3^{+1.9}_{-1.5}$
iPTF13bvn	r	$0.69^{+0.03}_{-0.03}$	$0.98^{+0.03}_{-0.03}$	$18.7^{+0.2}_{-0.2}$	$-17.24^{+0.12}_{-0.11}$	$11.9^{+0.7}_{-0.6}$	$6.5^{+1.9}_{-1.9}$
SN 2019odp	i	$0.37^{+0.02}_{-0.02}$	$0.33^{+0.02}_{-0.02}$	$13.8^{+0.2}_{-0.3}$	$-18.00^{+0.08}_{-0.09}$	$26.6^{+1.1}_{-1.2}$	$7.7^{+0.4}_{-0.3}$
SN 1998bw	Ic	$0.41^{+0.07}_{-0.06}$	$0.42^{+0.05}_{-0.05}$	$16.9^{+0.2}_{-0.1}$	$-19.34^{+0.08}_{-0.08}$	$21.2^{+2.0}_{-1.7}$	$6.1^{+1.8}_{-1.6}$
SN 2002ap	I	$0.58^{+0.05}_{-0.05}$	$0.45^{+0.02}_{-0.02}$	$18.5^{+0.2}_{-0.1}$	$-17.96^{+0.07}_{-0.07}$	$19.2^{+1.0}_{-1.1}$	$3.4^{+1.3}_{-0.6}$
SN 2008D	i	$0.43^{+0.02}_{-0.02}$	$0.41^{+0.01}_{-0.01}$	$20.6^{+0.4}_{-0.4}$	$-17.00^{+0.11}_{-0.13}$	$17.6^{+0.9}_{-1.1}$	$7.5^{+0.8}_{-0.5}$
iPTF13bvn	i	$0.58^{+0.03}_{-0.03}$	$0.79^{+0.03}_{-0.03}$	$16.7^{+0.4}_{-0.4}$	$-17.10^{+0.12}_{-0.10}$	$13.0^{+1.0}_{-0.9}$	$3.6^{+0.4}_{-0.4}$

Table 4. Basic lightcurve observables extracted for SN 2019odp and the comparison objects. Δm_{-10} denotes the magnitude difference from peak to 10 days before peak. Δm_{15} denotes the magnitude difference from peak to 15 days past peak. The linear slope is the late-time decline slope. M_{\max} denotes the peak absolute magnitude including extinction and distance uncertainties. Peak width denotes the width of the Gaussian around peak. The rise timescale denotes the timescale factor from the Contardo model.

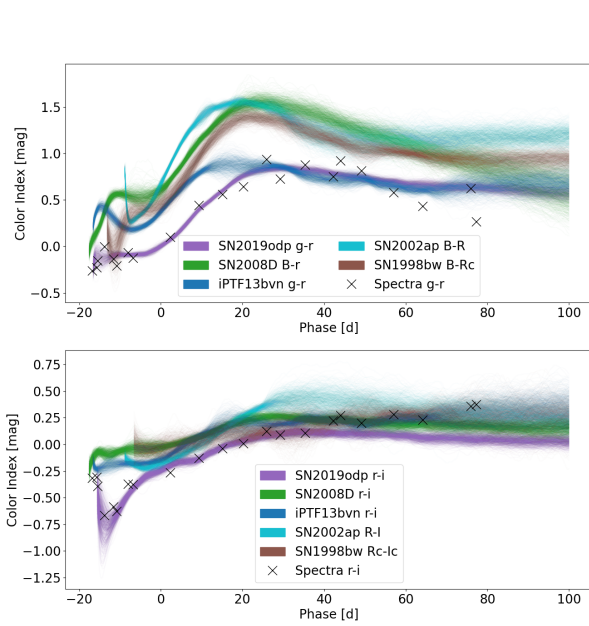


Fig. 5. Color evolution of SN 2019odp and the comparison objects. The top panel shows the $g - r$ color (or corresponding Johnson color). The lower panel shows $r - i$ color (or corresponding Johnson color). For each transient we sample 1000 realizations of the supernova lightcurve from the interpolation kernel. For SN 2019odp we also include synthetic photometry based on the observed spectra as a consistency check (using the same filter curve as the photometric dataset). They are denoted with black crosses.

may not be an uncommon feature for Type Ib supernovae. However both helium and iron have lines quite close in wavelength to those feature as well.

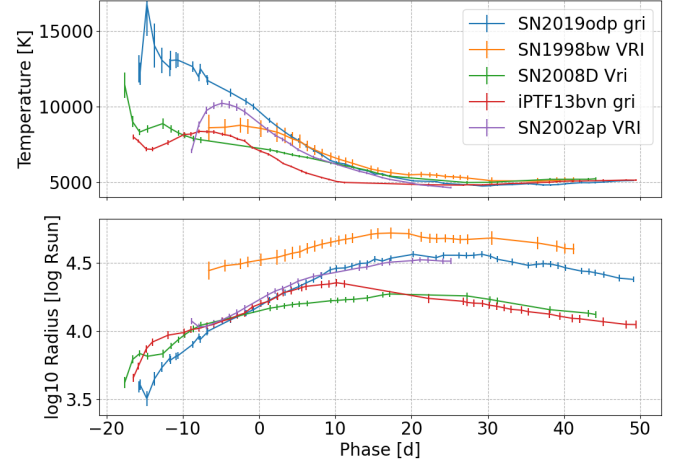


Fig. 6. Time evolution of the inferred blackbody parameters from the photometry for SN 2019odp and selected comparison objects. We chose the closest matching filter sets for all transients and performed our own fitting for all objects. The error bars contain all uncertainties including the distance and extinction uncertainties. The upper panel shows the temperature time-evolution and the lower panel the photospheric radius time-evolution.

We show the pre-nebular phase covering from +42d to +104d post-peak in Fig. 12. The calcium near-infrared triplet $\text{Ca II } \lambda\lambda 8498, 8542, 8662$ becomes the strongest emission feature in the spectrum, with some oxygen recombination features, such as $\text{O I } \lambda 7774$ also being quite pronounced. The helium features $\text{He I } \lambda\lambda 6678, 7065$ become less noticeable due to overlap with the broad oxygen doublet $[\text{O I}] \lambda\lambda 6300, 6364$ and the calcium doublet $[\text{Ca II}] \lambda\lambda 7291, 7324$.

We show the nebular phase spectra from +101d to +348d post-peak in Fig. 13. The most conspicuous emission features are the $[\text{O I}] \lambda\lambda 6300, 6364$ complex and the $[\text{Ca II}] \lambda\lambda 7292, 7324$ and $\text{Ca II } \lambda\lambda 8493, 8542, 8662$ lines. In the quasi-nebular spec-

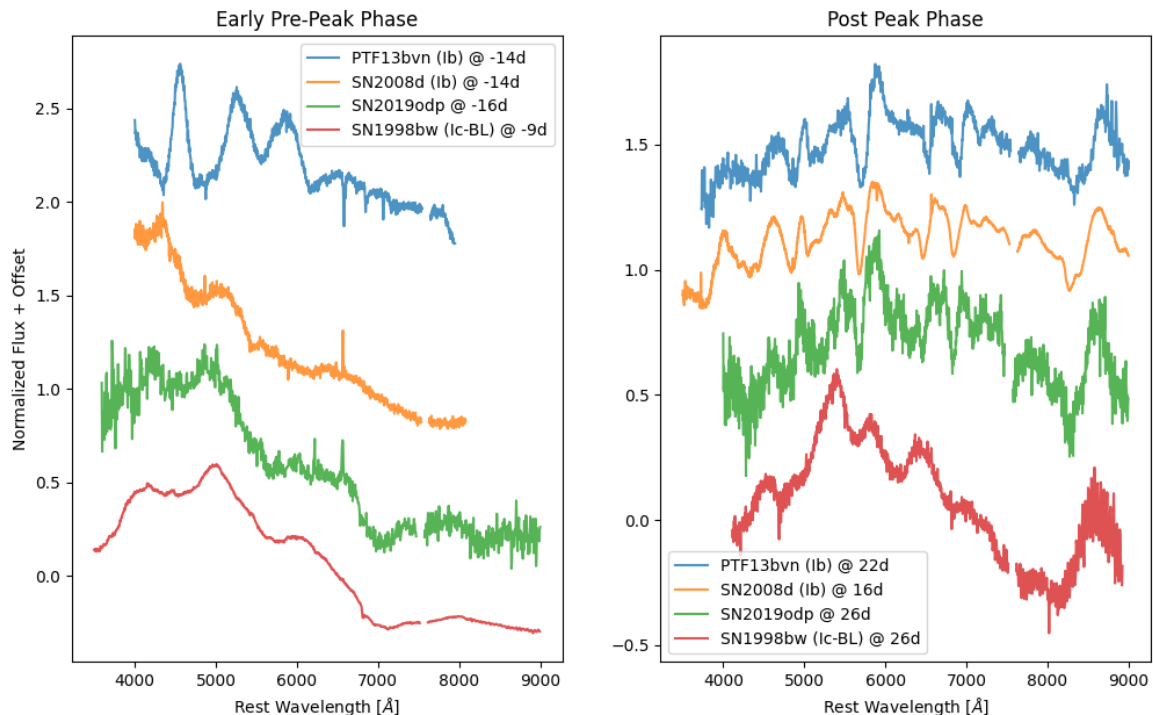


Fig. 7. Comparison of spectra of SN 2019odp before peak (left panel) and after peak (right panel) against selected comparison objects. The phases with respect to the respective g/V -band peak epochs are denoted in the legend. Telluric absorptions have been marked and masked, and the spectra are corrected for host extinction. At the early phase, the spectrum of SN 2019odp (the NTT classification spectrum) looks very much like the Type Ic-BL SN 1998bw (shown in red, Patat et al. 2001), and not at all like the typical Type Ib iPTF13bvn (shown in blue, Fremling et al. 2016). This is the reason for the initial classification on TNS as a Type Ic-BL supernova. However it looks quite similar to the Type Ib SN 2008D (shown in orange Shivvers et al. 2019; Modjaz et al. 2014), which has earlier observations than iPTF13bvn. At later phases (right panel), SN 2019odp is instead similar to typical Type Ib supernovae such as iPTF13bvn, showing narrower lines and clear helium features, as opposed to SN 1998bw. In fact, the most similar object might be the Type Ib SN 2008D. Some of the spectra suffer from host contamination.

tra there are also oxygen recombination lines visible at $O\text{I } \lambda\lambda 7772, 7774, 7775$, and $O\text{I } \lambda 8446$ and another feature at 9264 \AA . The oxygen lines show substantial structure, that complicates the measurements. The $\text{Mg I } \lambda 4571$ and $\text{Mg I } \lambda 5167$ lines become more pronounced. There is a quite pronounced Na I D line visible, which slowly replaces the $\text{He I } \lambda 5876$ feature.

The late-time Keck spectrum (+348d) is dominated by the $[\text{O I}] \lambda\lambda 6300, 6364$ complex, by $[\text{Ca II}] \lambda\lambda 7292, 7324$ and a little bit of emission of $\text{Mg I } \lambda 4571$. All other previously mentioned emission lines have vanished at this epoch.

We estimate the average $[\text{O I}]$ to $[\text{Ca II}]$ line-flux ratio to be in the range of 1.2–1.9, with the highest ratio being measured in the spectrum at +348d. When considering the velocity-resolved ratio the peak is 2.5 in the +349 d spectrum and 1.5 to 2.0 in the +128/+138 d spectra. This means that this transient belongs to the class of calcium-poor (or oxygen-rich) supernovae (Prentice et al. 2022) and is likely to have a more massive progenitor, since the oxygen emission is quite sensitive to the main-sequence mass, while the calcium emission is not (Limongi & Chieffi 2003).

3.7.1. Classification

As mentioned in Sect. 1.1, SN 2019odp was initially classified as a Type Ic-BL supernova by Brennan et al. (2019). When comparing the early spectra obtained shortly after discovery against

Type Ib (iPTF13bvn) and Type Ic-BL (SN 1998bw) supernovae (Fig. 7, left panel) it indeed seems quite suggestive to classify this supernova as a Type Ic-BL due to the overall structure of the continuum and the absence of obvious identifiable lines. Comparing against typical supernova databases used for classifications such as *SNID* (Blondin & Tonry 2007) supports this conclusion. However, later spectra (Fig. 7, right panel) showed the presence of lines with much smaller line widths than typically associated with Type Ic-BL supernovae as well as the presence of helium lines, which clearly showed that this is a Type Ib supernova.

Using our own classification database and code¹⁰ we searched for other supernovae that were a close spectral match for the early pre-peak spectra and found that the Type Ib SN 2008D is a quite good match (Fig. 7, left panel) as well. This suggests that this lack of features at early phases of the supernova is not completely unseen for Type Ib supernovae and additional care should be taken when classifying transients at very early phases.

It is not obvious if the lack of helium lines and broad spectral shape at early phases is due to very high velocities or due to other effects. Modjaz et al. (2016) argue that the lack of observed helium lines in Type Ic-BL supernovae cannot solely be explained

¹⁰ We implemented the spectral flattening/smoothing algorithm that *SNID* uses in python and implemented a simpler comparison metric given the known redshift of the supernova.

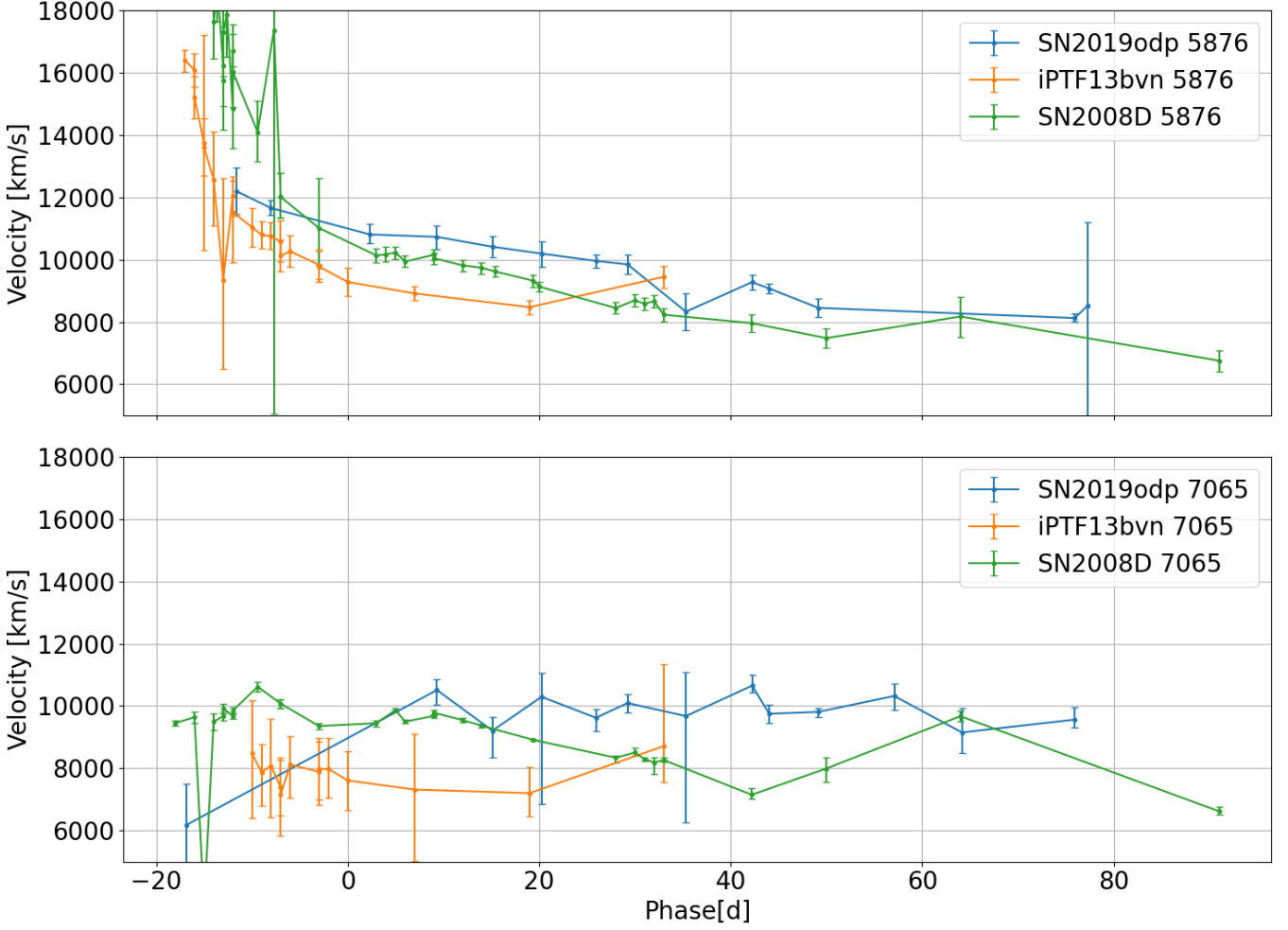


Fig. 8. Velocity Evolution of the He I lines in SN 2019odp and the comparison Type Ib supernovae.

by the helium lines being smeared out by the high velocities in the ejecta. Further transitional objects, such as SN 2016coi (Yamanaka et al. 2017; Prentice et al. 2018), have been discovered that show helium lines initially, but evolve to more closely resemble Type Ic-BL supernovae later on. This is the inverse to what is seen in SN 2008D and in SN 2019odp, where initially there was no visible helium lines, but they appeared later on. SN 2017ens (Chen et al. 2018) is another supernova showing characteristics of a Type Ic-BL supernova early on, but then changing its class to a Type II_n supernova. On the other hand there are normal Type Ib supernovae, such as iPTF13bvn, that have been discovered at similarly early phases that show no hints of broad lines. Bengyat & Gal-Yam (2022) argue for a split in the Type Ib class, which might explain these different behaviours.

3.7.2. Helium Velocity Evolution

We use the nested sampler *dynesty* to fit the following P-Cygni model function M_λ to the individual helium features:

$$M_\lambda = C_\lambda + E \mathcal{G}_\lambda(\Lambda + \Delta\Lambda_E, \sigma_E) - A \mathcal{G}_\lambda(\Lambda + \Delta\Lambda_A, \sigma_A), \quad (5)$$

where C_λ is the linear continuum function, \mathcal{G}_λ is the (normalized) Gaussian function, E is the amplitude of the emission feature, A is the amplitude of the absorption feature, Λ is the rest-wavelength of the feature, $\Delta_{A,E}$ are the velocity-offsets of the absorption and emission peak respectively and, $\sigma_{A,E}$ are the widths

of the absorption/emission Gaussians. The measured velocity evolution for SN 2019odp and the comparison Type Ib supernovae are shown in Fig. 8.

We estimate the He I $\lambda 5876$ line velocity at peak by fitting the following exponential model to the individual velocity estimates using a GP kernel as likelihood function:

$$v_{\text{abs}}(t) = v_0 \exp(t - t_0)^\alpha, \quad (6)$$

where v_0 , t_0 and α are free parameters (within reasonably chosen priors). We only include significant measurements in the time range from -15.5 d to 30 d. Our estimate for the absorption velocity at peak is thus:

$$v_{\text{abs}}(\text{He I } 5876\text{\AA}) = 10977 \pm 400 \text{ km s}^{-1} \quad (7)$$

4. Modelling

4.1. Photospheric Phase

During the photospheric phase of the supernova the ejecta is assumed to be optically thick. We first introduce the models under consideration, followed by a description of the parameter estimation methods and then present the derived parameters of all models in the final sub section.

4.1.1. Arnett Model Description

The most used analytic model for estimating ejecta properties for supernovae from the lightcurve peak is the [Arnett \(1982, hereafter A82\)](#) model. The model is based on the following assumptions:

1. Homologous expansion of the ejecta:

$$R(t) \simeq R(t=0) + v_{sc} t \quad (8)$$

2. The ejecta is a radiation-dominated gas
3. The diffusion approximation applies
4. The opacity κ_{opt} is constant throughout the ejecta and also constant in time
5. Spherical symmetry
6. Volume emission of radioactive decay energy is proportional to the radiation energy per unit volume.

Apart from these assumptions further approximations can be made, such as the commonly used approximation that the initial radius $R(t=0)$ is small and thus $R(t) \simeq v_{sc} t$.

Using the formalism from [Khatami & Kasen \(2019, their eq. 11¹¹\)](#) we can state the luminosity as follows:

$$L(t) = \frac{2}{\tau_m^2} \exp^{-(t/\tau_m)^2} \int_0^t t' Q_{dep}(t') \exp^{(t'/\tau_m)^2} dt', \quad (9)$$

where τ_m is the diffusion timescale and $Q_{dep}(t)$ is the time-dependant heating term.

The diffusion timescale relates to the ejecta mass and scale-velocity v_{sc} in the following way ([Arnett 1982, eqs. 18 and 22](#)):

$$\tau_m^2 = \frac{2\kappa_{opt} M_{ej}}{\beta c v_{sc}}, \quad (10)$$

where M_{ej} is the ejecta mass, β is a density-profile integration constant and κ_{opt} is the opacity.

Since the scale velocity is not a quantity that can be measured directly we need to find some proxy for it. We can use the “representative” mean expansion rate v_m from [Dessart et al. \(2016\)](#) to try to estimate the mean-squared velocity $\langle v^2 \rangle$ in the Arnett model:

$$\langle v^2 \rangle = v_m^2 = \frac{2E_K}{M_{ej}}, \quad (11)$$

where E_K is the total kinetic energy of the explosion.

We use [Arnett \(1980, their eqn. 31\)](#) to relate the mean-square velocity to the scale velocity:

$$\langle v^2 \rangle = \zeta^2 v_{sc}^2, \quad (12)$$

where ζ is a density-profile dependent integration constant¹².

¹¹ We use Q_{dep} instead of L_{heat} and τ_m instead of τ_d .

¹² [Arnett \(1980\)](#) calculate $\zeta^2 \equiv I_K/I_M$ for uniform and different exponential density distributions. [Liu et al. \(2018\)](#) provides analytic expressions for broken power-law distributions.

We use the following relation between He I $\lambda 5876$ line velocity v_{abs} (see [Sect. 3.7.2](#)) and the mean expansion velocity v_m from [Dessart et al. \(2016, their sec. 5.3\)](#):

$$\frac{v_{abs}(\text{He I } \lambda 5876)}{1000 \text{ km s}^{-1}} = 2.64 + 0.765 \frac{v_m}{1000 \text{ km s}^{-1}}, \quad (13)$$

we estimate the expansion velocity of SN 2019odp at light curve peak to be $v_m = 10912 \pm 1435 \text{ km s}^{-1}$.

Thus the ejecta mass and kinetic energy can be given in terms of the mean expansion rate v_M :

$$M_{ej} = \frac{\tau_m^2 \beta c v_M}{2\zeta \kappa_{opt}} \quad (14)$$

$$E_K = \frac{\tau_m^2 \beta c v_M^3}{4\zeta \kappa_{opt}} \quad (15)$$

Assuming a power-law density profile (with a limited range of the power-law index around uniform density) we approximate β/ζ as a constant value (17.8 for this paper¹³), and adopt a mean opacity $\kappa_{opt} = 0.07 \text{ cm}^2 \text{ g}^{-1}$.

Description	Symbol	Value
^{Ni} 56 Lifetime	τ_{Ni}	8.77 d
^{Co} 56 Lifetime	τ_{Co}	111.45 d
^{Ni} 56 Decay Lum.	q_{Ni}	$6.45 \times 10^{43} \text{ erg } M_{\odot}^{-1} \text{ s}^{-1}$
^{Co} 56 Gamma Decay Lum.	$q_{Co,\gamma}$	$1.38 \times 10^{43} \text{ erg } M_{\odot}^{-1} \text{ s}^{-1}$
^{Co} 56 Positron Decay Lum.	q_{Co,e^+}	$4.64 \times 10^{41} \text{ erg } M_{\odot}^{-1} \text{ s}^{-1}$

Table 5. Nuclear decay constants from [Wygoda et al. \(2019\)](#) used in the radioactive decay chain heating function.

We use the formalism for the heating function from [Wygoda et al. \(2019\)](#) for the radioactive decay heating of ^{Ni}56 and ^{Co}56 (their eqn. 11 and 12):

$$Q_{\gamma}(t) = M_{Ni} (q_{Ni} \exp^{-t/\tau_{Ni}} + q_{Co,\gamma} \exp^{-t/\tau_{Co}}) \quad (16)$$

$$Q_{e^+}(t) = M_{Ni} q_{Co,e^+} (\exp^{-t/\tau_{Co}} - \exp^{-t/\tau_{Ni}}), \quad (17)$$

where ϵ_{Ni} is the specific heating rate for Nickel decays, $\epsilon_{Co,\gamma}$ is the gamma-ray specific heating rate for Cobalt decays, ϵ_{Co,e^+} is the positron specific heating rate for Cobalt decays, $\tau_{Ni,Co}$ are the decay timescales. The used physical constants for the heating function(s) are summarized in [Table 5](#). The total heating function is given by:

$$Q_{dep}(t) = Q_{\gamma}(t) + Q_{e^+}(t) \quad (18)$$

We use the parameter estimating method described in [Sect. 4.1.3](#). The used priors for the model are shown in [Table 6](#). Since the model does not contain any treatment for gamma-ray leakage we restrict the fitting range to roughly the diffusion timescale. The resulting parameter estimates for SN 2019odp and the comparison objects for all models are shown in [Table 7](#) (we also include literature values where available as a consistency check).

¹³ This corresponds to the often used $\beta = 13.8$ and $\zeta^2 = \frac{3}{5}$ for uniform density.

4.1.2. Large Initial Radius

Another variant of the A82 model does not assume a negligible initial radius $R_0 \equiv R(t=0)$.

Introducing an additional timescale:

$$\tau_r = \frac{v_{sc} \tau_m^2}{2R_0} \quad (19)$$

and then following the approach from [Chatzopoulos et al. \(2012\)](#) (but using the more generalized notation from before) we get the following function for the luminosity:

$$L(t) = \frac{2}{\tau_m^2} \exp^{-t^2/\tau_m^2 - t/\tau_r} \int_0^t \left(t' + \frac{R_0}{v_{sc}}\right) Q_{\text{dep}}(t') \exp^{t'^2/\tau_m^2 + t'/\tau_r} dt' \quad (20)$$

4.1.3. Fitting Framework

We here compare the different models using a bayesian framework. We use the python nested sampling framework *dynesty* to both estimate the posterior as well as the evidence of the different models under consideration. The methodology includes propagating all the correlated uncertainties into the derived posterior, and is insensitive to time-range selection effects, due to the changing number of observational data points included in the fit.

In the likelihood function we sample the bolometric lightcurve based on the interpolated lightcurves¹⁴ and each sampled lightcurve contains the correlated uncertainties mentioned above. Each sampled lightcurve consists of 50 sample points randomly sampled within the defined model time-range (with some further constraints imposed by the underlying observations).

Even though the number of sample points is fixed the information content is not. In the most extreme case the 50 points may only span the time range of one day, in which case most models will fit reasonably well.

4.1.4. Results

We summarize the parameter estimation results in [Table 7](#), where we also include values from the literature for the comparison objects. Compared to other samples of Type Ib supernovae, such as [Taddia et al. \(2018\)](#) or [Lyman et al. \(2016\)](#), SN 2019odp is near the edge of the distribution, but there are objects in these samples that have similar ejecta masses ($M_{\text{ej}} \sim 5 M_{\odot}$) and nickel masses ($M_{\text{Ni}} \sim 0.25 M_{\odot}$). However the inferred kinetic energy ($E_K \sim 6 \times 10^{51}$ erg) is significantly higher than for other Type Ib supernovae and is more comparable to values seen in Type Ic-BL supernovae. While the models including an initial radius R_0

¹⁴ Since the likelihood function is evaluated millions of times during the nested sampling process we pre-generate 12000 samples of the interpolated lightcurve and then randomly select among them in the likelihood function.

Parameter	Symbol	Unit	Prior
Nickel Mass	$M(\text{Ni}^{56})$	M_{\odot}	$\mathcal{U}(0.01, 1.4)$
Diffusion Timescale	τ_m	d	$\mathcal{U}(5, 55)$
Explosion Epoch	t_{expl}	d	$\mathcal{U}(t_{\text{min}}, t_{\text{detect}})$

Table 6. Priors for the small R_0 Arnett model Fit. The root-mean-square velocity values are different per object: For SN 2019odp the value can be found in [Sect. 3.7.2](#) and for the comparison objects they are taken from [Table 3](#). For SN 2019odp we use the explosion epoch prior given in [Sect. 1.1](#) and for the comparison objects the one listed in [Table 3](#).

are not very constraining they do rule out things like super-giant stars and point more towards compact objects as a progenitor. We investigate the progenitor radius in the context of shock cooling models in [Sect. 4.2](#).

For comparison purposes we also calculate the ejecta mass and kinetic energy under the (often used) assumption of $v_{sc} = v_{\text{ph}}(t_{\text{peak}})$. This yields a lower ejecta mass of $\sim 4.2 M_{\odot}$ and kinetic energy of $\sim 3.8 \times 10^{51}$ erg. We note that both estimates exceed the values commonly derived in theoretical works for neutrino driven explosions, which do not exceed an explosion energy of around $2 - 3 \times 10^{51}$ erg ([Ertl et al. 2020](#)).

4.2. Early Plateau

As noted in [Sect. 3.3](#), the first few observations show an excess or plateau rather than a smoothly rising lightcurve. Other supernovae that have showed an early excess or lightcurve ‘‘bump’’ include the Type Ib XRF-SN 2008D, the Type Ic-BL GRB-SN 2006aj and the Type IIb SN 2016gkg ([Tartaglia et al. 2017](#); [Arcavi et al. 2017](#)). Common features among these three are blue colors, strong UV emission, high temperatures ($T \gtrsim 12000$ K) that is decreasing right from discovery, and the early excess is shaped like an additional (usually smaller) early peak in the lightcurve. While SN 2019odp does show a very blue color ([Sect. 3.4](#); [Fig. 5](#)) and high temperatures early on ([Sect. 3.5](#); [Fig. 6](#)), it neither shows strong UV emission initially (the $U - r$ color in fact gets bluer instead of redder) nor is the initial lightcurve similar (no early peak, but an actual plateau; [Sect. 3.3](#)).

One commonly invoked scenario to explain this early excess is shock cooling emission ([Chevalier & Fransson 2008](#); [Arcavi et al. 2017](#)). Several (semi-)analytical shock cooling emission models have been developed to explore the UV/optical lightcurve ([Nakar & Sari 2010](#); [Rabinak & Waxman 2011](#); [Piro et al. 2021](#)). As the shock cools, at some point the temperature will drop below the recombination temperature of the shocked material ([Dessart et al. 2011](#); [Rabinak & Waxman 2011](#)) and then the luminosity starts to plateau until radioactive energy input becomes significant ([Piro & Nakar 2013](#)). Since we do not see any excess UV emission in SN 2019odp and the luminosity plateaued right after discovery, we conclude that in this scenario we have missed the shock cooling emission itself and are only seeing emission from the recombination phase. Based on the numerically recalibrated shock model by [Nakar & Sari \(2010\)](#), [Piro & Nakar \(2013\)](#) use the plateau luminosity and explosion parameters to estimate the progenitor radius R_0 (their eqn. 5 solved for R_0):

$$R_0 \approx \left(\frac{L_P}{7 \times 10^{40} \text{ ergs}^{-1}} \frac{\left(\frac{\kappa}{0.2 \text{ cm}^2 \text{ g}^{-1}}\right)^{0.69} \left(\frac{M_{\text{ej}}}{1 M_{\odot}}\right)^{0.67}}{\left(\frac{E_K}{10^{51} \text{ erg}}\right)^{0.85}} \right)^{1.28} R_{\odot} \quad (21)$$

The predicted start of the plateau after the explosion for a $< 10 R_{\odot}$ progenitor and the estimated explosion parameters in [Sect. 4.1.1](#) is between 20 hours and 4 days - both of which fit easily in the observation gap before first light. Using the estimated plateau luminosity ([Sect. 3.6](#)) we use [Equation 21](#) to estimate the progenitor radius to be $0.6 - 1.4 R_{\odot}$. This is comparable to the estimate of $R_0 \approx 2 R_{\odot}$ for SN 2008D by [Rabinak & Waxman \(2011\)](#). This value is also compatible with the upper limit of $18 R_{\odot}$ ([Table 7](#)) derived using the large-radius formulation of the Arnett equation ([Sect. 4.1.2](#)).

Another possible scenario is imperfect mixing of the nickel throughout the ejecta ([Yoon et al. 2019](#)). Depending on the mix-

SN Name	Model/Reference	Phase fitted (d)	τ_m (d)	$M(\text{Ni}^{56})$ (M_\odot)	M_{ej} (M_\odot)	E_K (10^{51} erg)	$R(t=0)$ (R_\odot)
SN2019odp	A82-c	-11 – 25	18.7 ± 2	0.246 ± 0.04	5.4 ± 1.5	6.4 ± 1.5	
SN2019odp	A82-e	-11 – 25	18.9 ± 2	0.253 ± 0.04	5.7 ± 1.2		9_{-9}^{+9}
iPTF13bvn	Lyman et al. (2016)	-9 – 10	$12.5 - 13.4$	$0.06_{-0.01}^{+0.02}$	$1.7_{-0.4}^{+0.5}$	$0.7_{-0.2}^{+0.3}$	
iPTF13bvn	A82-c	-13 – 30	11.8 ± 1.2	0.0676 ± 0.02	1.6 ± 0.4	1.1 ± 0.3	
iPTF13bvn	A82-e	-15 – 25	12.3 ± 1.1	0.0746 ± 0.02	1.8 ± 0.3		8_{-8}^{+7}

Table 7. Parameter Estimation Results. We also include literature comparison values in this table (paper reference takes the place of the model name). The models are: **A82-c** (c for compact) for small R_0 and **A82-e** (e for extended) for large R_0 .

ing fraction they argue that different lightcurve plateaus or “pre-bumps” are possible. Lack of nickel in the outer part of the ejecta would also be consistent with the helium absorption lines only becoming visible later on (Sect. 3.7) due to the lack of nonthermal excitation of the helium by the nickel decays (Lucy 1991). Taddia et al. (2015) explores plateau duration, luminosity and magnitude difference to peak ($\Delta M \equiv M_{\text{plat}} - M_{\text{peak}}$) using a small grid of hydrodynamical models. While the inferred ejecta mass and energy for SN 2019odp (Sect. 4.1.4) fall far outside the model grid, the observed plateau duration of 2 – 5 d, plateau luminosity $\log L_{\text{plat}} = 41.3$ [$\log(\text{erg s}^{-1})$] and magnitude difference $\Delta M \approx 3.3$ mag (Sect. 3.6), fall well into the range of values seen in their model grid. Extrapolating the trend seen for the ejecta mass and nickel mixing beyond the model grid suggests that very low nickel mixing scenarios are not an obvious candidate, since both low nickel mixing and high ejecta mass increase the duration of the plateau.

4.3. Constraining the Oxygen Mass

The progenitors of supernova explosions directly connect to stellar evolution models and the different channels leading to the supernova (binary stars vs. massive stars for example). One technique to estimate the Zero-Age Main Sequence (ZAMS) mass of the progenitor is to use the oxygen mass as a proxy, as it has good sensitivity to the pre-explosion mass in simulations (Limongi & Chieffi 2003; Heger & Woosley 2010). A method to estimate an upper limit on the oxygen mass is described in Jerkstrand et al. (2014). For this we integrate the flux in a 100 Å window around the [O I] $\lambda 5577$ line and the [O I] $\lambda \lambda 6300, 6364$ lines¹⁵ while subtracting a background baseline. Based on these line luminosities we estimate a lower limit for the temperature of 3888 K and an upper limit of $4 M_\odot$ for the oxygen mass. While this value does not conflict with the previously estimated total ejecta mass, it is a quite significant fraction and only a few transients have previously been estimated to have such large oxygen masses.

Thus we expand upon the method used in Jerkstrand et al. (2014). We first describe the analytic models we use in Sect. 4.3.1, and in Sect. 4.3.2 we describe the fitting method employed to actually apply the improved model. In Sect. 4.3.3 we describe the results of this methodology.

4.3.1. Model Description

The most important oxygen emission lines for this are the [O I] $\lambda \lambda 6300, 6364$ ($u_1 = 2s^2 2p^4(^1D) \rightarrow g = 2s^2 2p^4(^3P)$) doublet lines as well as the [O I] $\lambda 5577$ ($u_2 = 2s^2 2p^4(^1S) \rightarrow u_1 = 2s^2 2p^4(^1D)$) line. In the Sobolev approximation and assuming

¹⁵ With the range starting 50 Å blueward of 6300 Å and ending 50 Å redward of 6364 Å.

a uniform density distribution the total line luminosity for the transition λ ($u \rightarrow l$) is given by (Jerkstrand 2017):

$$L_\lambda = N_u A_\lambda h \frac{c}{\lambda} \beta_\lambda, \quad (22)$$

where A_λ is the radiative decay rate for the transition, β_λ is the Sobolev escape probability and, N_u is the total number of ions in the excited state u .

The first difference in our method is that we treat the two [O I] $\lambda \lambda 6300, 6364$ doublet lines separately. Since both share the same source state and only differ in the split ground-state (which is in LTE) they only differ by the radiative decay rate A as well as in the escape probability β . We assume all oxygen line emission to come from the same environmental conditions and thus we can state the [O I] $\lambda 6364$ optical depth in terms of the [O I] $\lambda 6300$ optical depth (Elmhamdi 2011):

$$\tau_{6364} = \frac{\tau_{6300}}{3} \quad (23)$$

Since we fit both lines of the doublet simultaneously we can use the amplitude ratio between the two lines to constrain the optical depth of both lines. This replaces the fixed assumption of $\beta_{6300,6364} \approx 0.5$ ($\tau_{6300,6364} \approx 2$) in Jerkstrand et al. (2014). We specify all optical depths in relation to the [O I] $\lambda 6300$ optical depth: $\tau \equiv \tau_{6300}$.

The Sobolev escape probability β in terms of the optical depth τ is defined as follows (Jerkstrand 2017):

$$\beta_\lambda = \frac{1 - \exp^{-\tau_\lambda}}{\tau_\lambda} \quad (24)$$

Assuming LTE conditions we can approximate the excited state numbers as follows (Jerkstrand 2017):

$$N_u = N \frac{g_u}{Z(T)} \exp \frac{-E_u}{k_B T}, \quad (25)$$

where N is the total number of atoms/ions, g_u is the statistical weight of the excited state, $Z(T)$ is the partition function and E_u is the energy level of the excited state. In the case of state u_2 we allow this population number to fall below the LTE estimate ($N_2^{\text{LTE}} \rightarrow d_2 N_2^{\text{LTE}}$ where d_2 is the LTE departure coefficient). Temperatures in the emission regions in the nebular phase are typically assumed to be below 5000 K. We adopt a more conservative prior range of 1000 – 8000 K, since it is difficult to define any particular cut-off point for the temperature.

We approximate the partition function with the statistical weight g_g of the ground state¹⁶ and state the equation in terms

¹⁶ Below $T_e = 1$ eV this is a quite good approximation, since the partition function is dominated by the split ground state.

of oxygen mass M_{OI} using $N = M_{\text{OI}} \mu^{-1} m_p^{-1}$ and restate the line luminosities:

$$L_\lambda = \Lambda_\lambda \frac{\beta_\lambda M_{\text{OI}}}{\exp(T_\lambda/T)}, \quad (26)$$

where $T_\lambda = \frac{E_u}{k_B}$ and all the physical constants are contained in Λ_λ .

$$\Lambda_\lambda = \frac{A_\lambda h c g_u}{\mu m_p \lambda g_g}, \quad (27)$$

where $\mu = 16$ is the mean atomic weight of oxygen, m_p is the mass of the proton, A_λ is the radiative decay rate of the transition, g_u is the statistical weight of the upper state and g_g is the statistical weight of the lower state.

If we assume the first excited state u_1 to be in LTE we can state the optical depth of [O I] $\lambda 5577$ relative to the [O I] $\lambda 6300$ optical depth:

$$\frac{\tau_{5577}}{\tau} = \frac{g_2 d_2 A_{5577} 5577^3}{g_1 A_{6300} 6300^3} \exp\left(\frac{E_1}{k_B T}\right) \frac{1 - \exp\left(-\frac{\Delta E_{2 \rightarrow 1}}{k_B T}\right)}{1 - \exp\left(-\frac{E_1}{k_B T}\right)}, \quad (28)$$

where d_2 is the NLTE deviation fraction for the second excited state u_2 and $\Delta E_{2 \rightarrow 1} = E_2 - E_1$. In [Jerkstrand et al. \(2014\)](#) the analog for this is the assumed ratio of $\beta_{5577}/\beta_{6300,6364} \approx 1.5$. The LTE departure coefficient denotes by how much the number density of the u_2 state falls below the LTE estimate. [Jerkstrand et al. \(2014\)](#) find a range for d_2 of 0.8 to 0.3 over the time range of 250 to 450 days post-explosion from their modelling efforts for Type IIP supernovae. We adopt a prior range of 0.1 – 1.0 for d_2 .

Combined with [Equation 24](#) we can calculate $\beta_{5577}(d_2, T, \tau)$ and state the [O I] $\lambda 5577$ line luminosity as follows (based on [Jerkstrand et al. 2014](#), their eqn. 2):

$$\frac{L_{5577}}{L_{6300}} = d_2 \frac{g_{u_2}}{g_{u_1}} \cdot \exp\left(-\frac{\Delta E_{2 \rightarrow 1}}{k_B T}\right) \frac{A_{5577} \beta_{5577}(d_2, T, \tau) 6300}{A_{6300} \beta_{6300} 5577} \quad (29)$$

$$= d_2 \cdot 51 \cdot \exp^{-25789.8/T} \frac{\beta_{5577}(d_2, T, \tau)}{\beta_{6300}}, \quad (30)$$

with the physical constants given in [Table 8](#).

4.3.2. Fitting Method

While our method adds to [Jerkstrand et al. \(2014\)](#), it does require knowing the line profile function \mathcal{P} . This stems from the need of disentangling the flux from the [O I] $\lambda 6300$ and the [O I] $\lambda 6364$ lines, which overlap due to the large velocities present in supernovae. We estimate the line fluxes $\{F\}$ using empirical spectral models, and then use those measurements to derive the physical parameter vector θ we are actually interested in.

We use the nested sampler *dynesty* to fit the parameter vector Ξ . Since in the early nebular spectra the O I $\lambda 7774$ recombination line is still present, we use this line to estimate the line profile of the forbidden oxygen lines for those epochs. We project a section around the O I $\lambda 7774$ line into velocity space, normalize it and then use it as an empirical line profile function \mathcal{P}_λ . For the last (+348 d) spectrum the recombination line is no longer visible and we use a parametric Gaussian as the line profile function instead:

$$\mathcal{P}_\lambda = \mathcal{G}_\lambda(\lambda_c, \sigma) \quad (31)$$

To this central line profile function \mathcal{P} we add a thick shell function \mathcal{S} to model any additional emission in the outer regions

of the supernova ejecta, since the simple Gaussian does not capture all of the flux of the line complex:

$$\mathcal{P}'_\lambda(\lambda_c, \Xi) = F_{6300} \mathcal{P}_\lambda(\lambda_c, \Xi) + F_{\text{shell}} \mathcal{S}_\lambda(\lambda_c, \Xi), \quad (32)$$

where F are the line fluxes. The line profile function for the thick shell is approximated by an elongated Gaussian function:

$$\mathcal{S}_\lambda(\lambda_c, \Xi) = \frac{1}{k} \frac{1}{\sigma \sqrt{2\pi}} \begin{cases} \exp\left(-\frac{(\lambda - \lambda_c + \lambda_s)^2}{2\sigma^2}\right) & \lambda \leq -\lambda_s \\ \exp\left(-\frac{(\lambda - \lambda_c - \lambda_s)^2}{2\sigma^2}\right) & \lambda \geq \lambda_s \\ 1 & -\lambda_s < \lambda < \lambda_s \end{cases}, \quad (33)$$

where λ_c is the center position, λ_s is the elongation width (corresponds to the inner cut-off velocity of the shell), σ is the Gaussian width (corresponds to the width of the shell), and k is the numerically derived normalization constant.

We segment the spectra into two spectral regions: the [O I] $\lambda 5577$ region and the [O I] $\lambda \lambda 6300, 6364$ region. These line profile functions are then (re)projected onto the observed wavelength grid around the [O I] $\lambda 5577$ region and the [O I] $\lambda \lambda 6300, 6364$ regions. We allow for a global wavelength offset $\Delta\lambda$. For the [O I] $\lambda \lambda 6300, 6364$ region we have the following model spectral flux function:

$$M_{\lambda - \Delta\lambda}(\Xi) = \mathcal{P}'_\lambda(6300, \Xi) + \mathcal{R}_6 \mathcal{P}'_\lambda(6364, \Xi) + C_\lambda, \quad (34)$$

with $\mathcal{R}_6 \equiv F_{6364}/F_{6300}$, which is constrained to the range between fully optically thin ($\mathcal{R}_6 = 1/3$) and fully optically thick ($\mathcal{R}_6 = 1$). For the [O I] $\lambda 5577$ region we have the following model spectral flux function:

$$M_{\lambda - \Delta\lambda}(\Xi) = \mathcal{R}_5 \mathcal{P}'_\lambda(5577, \Xi) + C_\lambda, \quad (35)$$

with $\mathcal{R}_5 \equiv F_{5577}/F_{6300}$. For each region we assume a separate linear continuum:

$$C_\lambda = \alpha_R + \beta_R \cdot (\lambda - \lambda_{\text{RC}}), \quad (36)$$

where λ_{RC} is the center of the region (5577 Å and 6330 Å respectively).

We marginalize over all nuisance parameters (all except the luminosities) to yield a 3 dimensional posterior distribution and calculate the mean and covariance matrix for this.

For the second stage Bayesian model the parameter vector θ only consists of a few parameters: the oxygen mass M_{OI} , temperature T , optical depth τ , distance D and the LTE departure coefficient d_2 . While this is quite a few more parameters than input values (which is just the three line fluxes) we are not aiming to constrain all of them, we are only really interested in the oxygen mass and marginalize over all the other parameters. This allows us to take into consideration any prior information for these parameters, without having to assume specific values. We use the equations in [Sect. 4.3.1](#). The priors on the physical parameters are stated in [Table 9](#). We use a multivariate Gaussian log-likelihood function, where we use the derived mean and covariance matrix from the previous stage. We then use the nested sampler *dynesty* to estimate the posterior distribution.

4.3.3. Results

We fit the three early to late nebular phase spectra (+128 d, +138 d, +348 d) using the algorithm and models described in [Sect. 4.3.2](#). The results of the first stage (spectral fitting) are summarized in [Table 10](#) and the detailed fitting results (corner plot and the line fits) can be found in [Sect. B.2](#). In the +348 d

Description	Symbol	Value	Unit
$2s^22p^4(^1S)$ Energy Level	E_2/k_B	48620	K
$2s^22p^4(^1D)$ Energy Level	E_1/k_B	22830	K
Statistical weight of u_2	g_{u_2}	1	
Statistical weight of u_1	g_{u_1}	5	
Statistical weight of ground state g	g_g	9	
Radiative Decay Rate of [O I] $\lambda 5577$	A_{5577}	1.26	s^{-1}
Radiative Decay Rate of [O I] $\lambda 6300$	A_{6300}	$5.63 \cdot 10^{-3}$	s^{-1}
Radiative Decay Rate of [O I] $\lambda 6364$	A_{6364}	$1.83 \cdot 10^{-3}$	s^{-1}

Table 8. Physical Constants used in the oxygen analysis. References: [Kramida et al. \(2021\)](#); [Jerkstrand et al. \(2014\)](#); [Jerkstrand \(2017\)](#).

Parameter	Symbol	Unit	Prior
Oxygen Mass	M_{O_1}	M_\odot	$\mathcal{U}(0, 6)$
Oxygen Temperature	T	K	$\mathcal{U}(1000, 8000)$
Distance	D	cm	$\mathcal{U}(D_{\min}, D_{\max})$
[O I] $\lambda 6300$ Opt. Depth	$\log \tau$		$\mathcal{U}(-5, 1)$
LTE Departure	d_2		$\mathcal{U}(0.1, 1)$

Table 9. Priors for the second stage of the oxygen mass estimation fit.

spectrum the detection of the [O I] $\lambda 5577$ line is only an upper limit and absent any secondary priors on the temperature or on the NLTE deviation we cannot constrain the oxygen mass.

Using the measured line fluxes, we then estimate the physical parameters. We show the posterior oxygen mass-temperature distributions for the +138 d and +348 d spectra in [Fig. 9](#). The detailed fitting results for the second stage of the procedure can be found in [Sect. B.3](#). While the distribution is fairly broad we can state without any additional constraints¹⁷:

$$\min M_{O_1}(T) = 0.47 M_\odot \quad (37)$$

This low oxygen mass limit corresponds to the high temperature end of our prior. The LTE departure coefficient of 0.1 corresponds to an electron number density n_e of around 10^7 cm^{-3} ([Maeda et al. 2007](#)). Assuming close to LTE conditions (and thus higher n_e and larger d_2) the minimum oxygen mass is above $3 M_\odot$. Since it is quite common in literature to just assume the temperature at the nebular phase to be in the range of 4000 – 5000 K, we include the minimum oxygen mass using the same assumption for comparison purposes:

$$\min_{T < 5000 \text{ K}} M_{O_1}(T) = 2.5 M_\odot \quad (38)$$

4.3.4. ZAMS Mass

We try to estimate the progenitor ZAMS mass based on different nucleosynthesis studies:

1. [Laplace et al. \(2021\)](#) compares the single massive star scenario to the binary evolution scenario and provides yields for both. In the massive star scenario the strict lower limit of the oxygen mass is compatible with all models more massive than $12 M_\odot$ (for $T_{O_1} < 5000 \text{ K} \rightarrow M_{\text{ZAMS}} \geq 21 M_\odot$). In the binary scenario all models more massive than $13 M_\odot$ are compatible with the oxygen mass (for $T_{O_1} < 5000 \text{ K}$ none

are compatible - the most massive model has $M_{O_1} \sim 2 M_\odot$). However none of the binary stripped star models less massive than $18 M_\odot$ are compatible with our ejecta mass estimate (since their pre-explosion mass is already below the ejecta mass). None of the massive stars are massive enough to fully strip their hydrogen.

2. [Woosley et al. \(1993\)](#) studies the evolution of 6 Wolf-Rayet models of varying ZAMS mass (35 – 85 M_\odot). While all models are consistent with the strict oxygen mass limit, only the $M_{\text{ZAMS}} > 35 M_\odot$ models manage to lose their hydrogen and are compatible with the inferred compact radius ([Sect. 4.2](#)) of the progenitor.
3. Assuming a binary-evolution model for Wolf-Rayet stars, [Dessart et al. \(2011\)](#) calculates several models for a ZAMS mass of $18 M_\odot$ and $25 M_\odot$, which produce from $0.5 M_\odot$ to $1.78 M_\odot$ of oxygen (however only one of the $25 M_\odot$ models matches the observed ejecta mass). Given the limited sampling of the model grid (5 models), this points to a ZAMS mass of $25 M_\odot$ (for $T_{O_1} < 5000 \text{ K} \rightarrow M_{\text{ZAMS}} > 25 M_\odot$).
4. Assuming a binary-evolution model for helium stars [Dessart et al. \(2020\)](#) calculates models for progenitor masses ranging from $4 M_\odot$ to $12 M_\odot$ (which corresponds to a ZAMS range of $14 - 32 M_\odot$) which cover an oxygen yield of $0.15 M_\odot$ to $1.84 M_\odot$. While all except the two least-massive models are consistent with our estimated oxygen mass (suggesting a M_{ZAMS} range of $23 - 36 M_\odot$), none of the models are consistent with the observed ejecta mass (the largest model has $M_{\text{ej}} = 3.69 M_\odot$). Assuming $T_{O_1} < 5000 \text{ K}$ none of the models are compatible with the higher oxygen limit.
5. Assuming a binary-evolution model for helium stars with mass-loss, [Ertl et al. \(2020\)](#) calculates explosion parameters for helium stars in the mass range $2.5 - 40 M_\odot$ (corresponds to $M_{\text{ZAMS}} = 13.5 - 91.7 M_\odot$). However since oxygen yield was only quantified averaged across models, we actually take the values from [Dessart et al. \(2021\)](#), which is based on the same models (except it is missing the models where $M_{\text{He}} > 12 M_\odot$). Based on the lower limit on the oxygen mass any helium star (M_{He}) more massive than $4.5 M_\odot$ ($T_{O_1} < 5000 \text{ K} \rightarrow M_{\text{He}} > 6 M_\odot$) is compatible. However only the two most massive helium star models **he8p0** ($M_{\text{He}} = 8 M_\odot, M_{\text{O}} = 1.7 M_\odot, M_{\text{ej}} = 4 M_\odot$) and **he12p0** ($M_{\text{He}} = 12 M_\odot, M_{\text{O}} = 3 M_\odot, M_{\text{ej}} = 5.3 M_\odot$) match both the oxygen mass estimate as well as the estimated total ejecta mass. This corresponds to a lower limit on the ZAMS mass of $28 - 35 M_\odot$. However our $M(\text{Ni}^{56})$ estimate is factor two higher than any model in [Ertl et al. \(2020\)](#).

5. Summary and Conclusions

We have presented photometric and spectroscopic observations of the peculiar Type Ib SN 2019odp.

¹⁷ Which we may have since the earlier nebular spectrum shows quite a number of other oxygen lines, which may be used to further constrain the temperature and/or the electron density. A qualitative estimate of the LTE departure coefficient d_2 based on oxygen recombination lines can be found in [Sect. B.1](#).

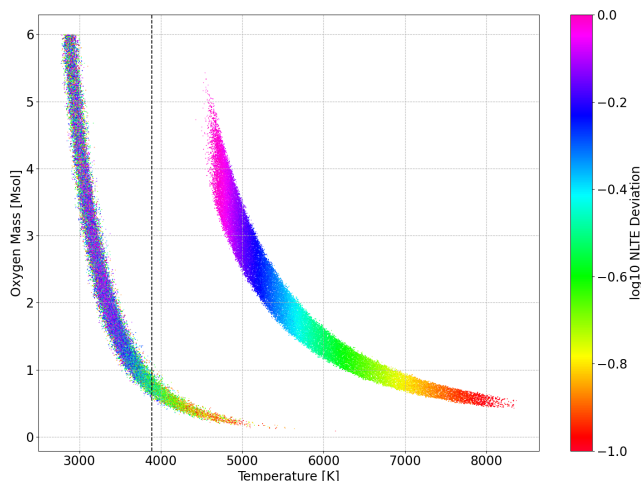


Fig. 9. Scatter plot of the marginalized posterior distribution showing the oxygen mass as function of the temperature for the last two observed spectra (the left-most trace corresponds to the very-late time spectrum at +348 d). The color denotes the LTE departure coefficient. One can see that the earlier spectrum provides a lower mass constraint, while the late one does not.

Line Phase	Luminosity +127.9d (10^{38} erg s $^{-1}$)	Luminosity +138.2d (10^{38} erg s $^{-1}$)	Luminosity +348.5d (10^{38} erg s $^{-1}$)
Profile Model	7774	7774	Gaussian
[O I] λ 5577	$13.5^{+7.9}_{-3.9}$	$26^{+21.9}_{-15.3}$	$0.18^{+0.58}_{-0.11}$
[O I] λ 6300	$127^{+29.5}_{-14.1}$	$129^{+40.8}_{-19.8}$	$8^{+4.1}_{-1.6}$
[O I] λ 6364	$44^{+10.9}_{-5.2}$	$44^{+22.2}_{-7.5}$	$3^{+2.33}_{-0.66}$

Table 10. Inferred line luminosities for the nebular phase spectra obtained. Distance uncertainty is folded in.

1. Based on the identification of helium absorption features in spectroscopic observations near peak we reclassify SN 2019odp to be a Type Ib supernova (Sect. 3.7.1). The pre-peak spectra however have great spectral similarity to Type Ic-BL supernovae as well as other transitional supernovae (SN 2008D, SN 2016coi, SN 2017ens). This may suggest a common scenario for all these supernovae early on.
2. Using optical photometric observations we construct a (pseudo-)bolometric lightcurve (Sect. 3.6) and estimate the peak luminosity to be $44^{+10}_{-7} \times 10^{41}$ erg s $^{-1}$ ($M_{\text{qbol}} \approx -17.9$ mag).
3. Using analytic bolometric lightcurve models we estimate the SN 2019odp ejecta mass to be $5.4 \pm 1.5 M_{\odot}$ with a Nickel yield of $0.25 \pm 0.04 M_{\odot}$ and a kinetic energy of $6.4 \pm 1.5 \times 10^{51}$ erg (Sect. 4.1.4).
4. We identify the presence of a pronounced plateau in the early lightcurve of 2 – 5 d in duration (Sect. 3.3) and $2.1^{+0.4}_{-0.4} \times 10^{41}$ erg s $^{-1}$ in luminosity (Sect. 3.6). Using analytic shock cooling models we identify this plateau as the recombination plateau following an undetected shock cooling peak (Sect. 4.2). Based on this we estimate the progenitor radius to be $\sim 1 R_{\odot}$.
5. We expand upon existing methods for estimating oxygen masses from nebular spectra and derive a strict range of $0.5 - 5 M_{\odot}$ for SN 2019odp (Sect. 4.3.3). Based on studies on single massive star evolution this points to a ZAMS

mass of $40 - 60 M_{\odot}$ – for binary star evolution to a ZAMS mass of $18 - 38 M_{\odot}$ (Sect. 4.3.4).

6. Many observational sample papers (Lyman et al. 2014; Taddia et al. 2018) have found rather low ejecta masses for Type Ib/Ic supernovae, which in combination with stellar evolution models hinted towards low ZAMS masses and binary progenitors for those objects. However due to the large inferred ZAMS mass for SN 2019odp the single massive star scenario cannot be ruled out.

Acknowledgements

We thank Jakob Nordin for additional comments. Based on observations obtained with the Samuel Oschin Telescope 48-inch and the 60-inch Telescope at the Palomar Observatory as part of the Zwicky Transient Facility project. ZTF is supported by the National Science Foundation under Grant No. AST-1440341 and a collaboration including Caltech, IPAC, the Weizmann Institute of Science, the Oskar Klein Center at Stockholm University, the University of Maryland, the University of Washington, Deutsches Elektronen-Synchrotron and Humboldt University, Los Alamos National Laboratories, the TANGO Consortium of Taiwan, the University of Wisconsin at Milwaukee, and Lawrence Berkeley National Laboratories. Operations are conducted by COO, IPAC, and UW. SED Machine is based upon work supported by the National Science Foundation under Grant No. 1106171. This work was supported by the GROWTH project (Kasliwal et al. 2019) funded by the National Science Foundation under Grant No 1545949. Part of the funding for GROND (both hardware as well as personnel) was generously granted from the Leibniz-Prize to Prof. G. Hasinger (DFG grant HA 1850/28-1). Based on observations made with the Nordic Optical Telescope, owned in collaboration by the University of Turku and Aarhus University, and operated jointly by Aarhus University, the University of Turku and the University of Oslo, representing Denmark, Finland and Norway, the University of Iceland and Stockholm University at the Observatorio del Roque de los Muchachos, La Palma, Spain, of the Instituto de Astrofísica de Canarias. Some of the data presented here were obtained in part with ALFOSC, which is provided by the Instituto de Astrofísica de Andalucía (IAA) under a joint agreement with the University of Copenhagen and NOT. Some of the data presented herein were obtained at the W. M. Keck Observatory, which is operated as a scientific partnership among the California Institute of Technology, the University of California and the National Aeronautics and Space Administration. The Observatory was made possible by the generous financial support of the W. M. Keck Foundation. M. W. Coughlin acknowledges support from the National Science Foundation with grant numbers PHY-2010970 and OAC-2117997. P. Rosnet acknowledges the support received from the Agence Nationale de Recherche of the French government through the program ANR-21-CE31-0016-03. This research has made use of the NASA/IPAC Infrared Science Archive, which is operated by the Jet Propulsion Laboratory, California Institute of Technology, under contract with the National Aeronautics and Space Administration. This research has made use of NASA’s Astrophysics Data System. The acknowledgements were compiled using the Astronomy Acknowledgement Generator. This research has made use of the NASA/IPAC Extragalactic Database (NED) which is operated by the Jet Propulsion Laboratory, California Institute of Technology, under contract with the National Aeronautics and Space Administration. This research has made use of the VizieR catalogue access tool, CDS, Strasbourg, France. This research

made use of Astroquery (Ginsburg et al. 2019). This research made use of Astropy, a community-developed core Python package for Astronomy (Astropy Collaboration et al. 2018, 2013). PyRAF is a product of the Space Telescope Science Institute, which is operated by AURA for NASA. This research made use of APLpy, an open-source plotting package for Python hosted at <http://aplpy.github.com>. This research made use of SciPy (Virtanen et al. 2020). This research made use of NumPy (Harris et al. 2020). IRAF is distributed by the National Optical Astronomy Observatory, which is operated by the Association of Universities for Research in Astronomy (AURA) under cooperative agreement with the National Science Foundation (Tody 1993). This research made use of matplotlib, a Python library for publication quality graphics (Hunter 2007). This work made use of the IPython package (Pérez & Granger 2007). We acknowledge the use of public data from the Swift data archive.

Data Availability

The final reduced and flux-calibrated spectra are available on WISEREP¹⁸ (Yaron & Gal-Yam 2012). The code and (most) data reduction inputs are available at <https://gitlab.com/welterde/ccsn-sn2019odp> (with a snapshot archived on Zenodo at <https://zenodo.org/record/7568627>). The data reduction products are available on Zenodo at <https://zenodo.org/record/7554926>.

References

- Aguado, D. S., Ahumada, R., Almeida, A., et al. 2019, *ApJS*, 240, 23
 Arcavi, I. 2022, *ApJ*, 937, 75
 Arcavi, I., Hosseinzadeh, G., Brown, P. J., et al. 2017, *ApJ*, 837, L2
 Arnett, W. D. 1980, *ApJ*, 237, 541
 Arnett, W. D. 1982, *ApJ*, 253, 785
 Astropy Collaboration, Price-Whelan, A. M., Sipőcz, B. M., et al. 2018, *AJ*, 156, 123
 Astropy Collaboration, Robitaille, T. P., Tollerud, E. J., et al. 2013, *A&A*, 558, A33
 Barbary, K. 2016, extinction v0.3.0
 Becker, A. 2015, HOTPANTS: High Order Transform of PSF ANd Template Subtraction
 Bellm, E. C., Kulkarni, S. R., Barlow, T., et al. 2019a, *PASP*, 131, 068003
 Bellm, E. C., Kulkarni, S. R., Graham, M. J., et al. 2019b, *PASP*, 131, 018002
 Bengyat, O. & Gal-Yam, A. 2022, *ApJ*, 930, 31
 Bertin, E., Mellier, Y., Radovich, M., et al. 2002, in *Astronomical Society of the Pacific Conference Series*, Vol. 281, *Astronomical Data Analysis Software and Systems XI*, ed. D. A. Bohlender, D. Durand, & T. H. Handley, 228
 Bianco, F. B., Modjaz, M., Hicken, M., et al. 2014, *ApJS*, 213, 19
 Blagorodnova, N., Neill, J. D., Walters, R., et al. 2018, *PASP*, 130, 035003
 Blanton, M. R. & Roweis, S. 2007, *AJ*, 133, 734
 Blondin, S. & Tonry, J. L. 2007, *ApJ*, 666, 1024
 Bradley, L., Sipőcz, B., Robitaille, T., et al. 2021, *astropy/photutils*: 1.2.0
 Breeveld, A. A., Landsman, W., Holland, S. T., et al. 2011, in *American Institute of Physics Conference Series*, Vol. 1358, *Gamma Ray Bursts 2010*, ed. J. E. McEnery, J. L. Racusin, & N. Gehrels, 373–376
 Brennan, S., Fraser, M., Ihanec, N., Gromadzki, M., & Yaron, O. 2019, *Transient Name Server Classification Report*, 2019-1595, 1
 Brown, P. J., Breeveld, A. A., Holland, S., Kuin, P., & Pritchard, T. 2014, *Ap&SS*, 354, 89
 Bruch, R. J., Gal-Yam, A., Schulze, S., et al. 2021, *ApJ*, 912, 46
 Cardelli, J. A., Clayton, G. C., & Mathis, J. S. 1989, *ApJ*, 345, 245
 Chambers, K. C., Magnier, E. A., Metcalfe, N., et al. 2016, *arXiv e-prints*, arXiv:1612.05560
 Chatzopoulos, E., Wheeler, J. C., & Vinko, J. 2012, *ApJ*, 746, 121
 Chen, T. W., Inserra, C., Fraser, M., et al. 2018, *ApJ*, 867, L31
 Chevalier, R. A. & Fransson, C. 2008, *ApJ*, 683, L135
 Clocciatti, A., Suntzeff, N. B., Covarrubias, R., & Candia, P. 2011, *AJ*, 141, 163
 Contardo, G., Leibundgut, B., & Vacca, W. D. 2000, *A&A*, 359, 876
 Dekany, R., Smith, R. M., Riddle, R., et al. 2020, *PASP*, 132, 038001
 Dessart, L., Hillier, D. J., Livne, E., et al. 2011, *MNRAS*, 414, 2985
 Dessart, L., Hillier, D. J., Sukhbold, T., Woosley, S. E., & Janka, H. T. 2021, *A&A*, 656, A61
 Dessart, L., Hillier, D. J., Woosley, S., et al. 2016, *MNRAS*, 458, 1618
 Dessart, L., Yoon, S.-C., Aguilera-Dena, D. R., & Langer, N. 2020, *A&A*, 642, A106
 Elmhamdi, A. 2011, *Acta Astron.*, 61, 179
 Ertl, T., Woosley, S. E., Sukhbold, T., & Janka, H. T. 2020, *ApJ*, 890, 51
 Filippenko, A. V. 1997, *ARA&A*, 35, 309
 Foley, R. J., Papekova, M. S., Swift, B. J., et al. 2003, *PASP*, 115, 1220
 Fremling, C., Sollerman, J., Taddia, F., et al. 2016, *A&A*, 593, A68
 Gehrels, N., Chincarini, G., Giommi, P., et al. 2004, *ApJ*, 611, 1005
 Ginsburg, A., Sipőcz, B. M., Brasseur, C. E., et al. 2019, *AJ*, 157, 98
 Graham, M. J., Kulkarni, S. R., Bellm, E. C., et al. 2019, *PASP*, 131, 078001
 Greiner, J., Bornemann, W., Clemens, C., et al. 2008, *PASP*, 120, 405
 Görtler, J., Kehlbeck, R., & Deussen, O. 2019, *Distill*, <https://distill.pub/2019/visual-exploration-gaussian-processes>
 Harris, C. R., Millman, K. J., van der Walt, S. J., et al. 2020, *Nature*, 585, 357
 Heger, A. & Woosley, S. E. 2010, *ApJ*, 724, 341
 Higson, E., Handley, W., Hobson, M., & Lasenby, A. 2019, *Statistics and Computing*, 29, 891
 Houck, J. C. & Fransson, C. 1996, *ApJ*, 456, 811
 Hunter, J. D. 2007, *Computing In Science & Engineering*, 9, 90
 Jerkstrand, A. 2017, in *Handbook of Supernovae*, ed. A. W. Alsabti & P. Murdin, 795
 Jerkstrand, A., Ergon, M., Smartt, S. J., et al. 2015, *A&A*, 573, A12
 Jerkstrand, A., Smartt, S. J., Fraser, M., et al. 2014, *MNRAS*, 439, 3694
 Jerkstrand, A., Smartt, S. J., Inserra, C., et al. 2017, *ApJ*, 835, 13
 Kasliwal, M. M., Cannella, C., Bagdasaryan, A., et al. 2019, *PASP*, 131, 038003
 Khatami, D. K. & Kasen, D. N. 2019, *ApJ*, 878, 56
 Kilpatrick, C. D., Drout, M. R., Auchettl, K., et al. 2021, *MNRAS*, 504, 2073
 Kramida, A., Yu. Ralchenko, Reader, J., & and NIST ASD Team. 2021, *NIST Atomic Spectra Database* (ver. 5.9), [Online]. Available: <https://physics.nist.gov/asd> [2022, March 17]. National Institute of Standards and Technology, Gaithersburg, MD.
 Krühler, T., Küpcü Yoldaş, A., Greiner, J., et al. 2008, *ApJ*, 685, 376
 Laplace, E., Justham, S., Renzo, M., et al. 2021, *A&A*, 656, A58
 Limongi, M. & Chieffli, A. 2003, *ApJ*, 592, 404
 Liu, L.-D., Zhang, B., Wang, L.-J., & Dai, Z.-G. 2018, *ApJ*, 868, L24
 Lucy, L. B. 1991, *ApJ*, 383, 308
 Lunnan, R., Chornock, R., Berger, E., et al. 2016, *ApJ*, 831, 144
 Lyman, J. D., Bersier, D., & James, P. A. 2014, *MNRAS*, 437, 3848
 Lyman, J. D., Bersier, D., James, P. A., et al. 2016, *MNRAS*, 457, 328
 Maeda, K., Tanaka, M., Nomoto, K., et al. 2007, *ApJ*, 666, 1069
 Masci, F. J., Laher, R. R., Rusholme, B., et al. 2019, *PASP*, 131, 018003
 Mazzali, P. A., Deng, J., Maeda, K., et al. 2002, *ApJ*, 572, L61
 Modjaz, M., Blondin, S., Kirshner, R. P., et al. 2014, *AJ*, 147, 99
 Modjaz, M., Gutiérrez, C. P., & Arcavi, I. 2019, *Nature Astronomy*, 3, 717
 Modjaz, M., Li, W., Butler, N., et al. 2009, *ApJ*, 702, 226
 Modjaz, M., Liu, Y. Q., Bianco, F. B., & Graur, O. 2016, *ApJ*, 832, 108
 Mould, J. R., Huchra, J. P., Freedman, W. L., et al. 2000, *ApJ*, 529, 786
 Nakar, E. & Sari, R. 2010, *ApJ*, 725, 904
 National Optical Astronomy Observatories. 1999, *IRAF: Image Reduction and Analysis Facility*, Astrophysics Source Code Library, record ascl:9911.002
 Nordin, J., Brinnet, V., Giomi, M., et al. 2019, *Transient Name Server Discovery Report*, 2019-1585, 1
 Oke, J. B., Cohen, J. G., Carr, M., et al. 1995, *PASP*, 107, 375
 Oke, J. B. & Gunn, J. E. 1982, *PASP*, 94, 586
 Patat, F., Cappellaro, E., Danziger, J., et al. 2001, *ApJ*, 555, 900
 Pérez, F. & Granger, B. E. 2007, *Computing in Science and Engineering*, 9, 21
 Perley, D. A. 2019, *PASP*, 131, 084503
 Piro, A. L., Haynie, A., & Yao, Y. 2021, *ApJ*, 909, 209
 Piro, A. L. & Nakar, E. 2013, *ApJ*, 769, 67
 Prentice, S. J., Ashall, C., Mazzali, P. A., et al. 2018, *MNRAS*, 478, 4162
 Prentice, S. J., Maguire, K., Siebenaler, L., & Jerkstrand, A. 2022, *MNRAS*, 514, 5686
 Prentice, S. J. & Mazzali, P. A. 2017, *MNRAS*, 469, 2672
 Puls, J., Vink, J. S., & Najarro, F. 2008, *A&A Rev.*, 16, 209
 Rabinak, I. & Waxman, E. 2011, *ApJ*, 728, 63
 Rigault, M., Neill, J. D., Blagorodnova, N., et al. 2019, *A&A*, 627, A115
 Roming, P. W. A., Kennedy, T. E., Mason, K. O., et al. 2005, *Space Sci. Rev.*, 120, 95
 Schlafly, E. F. & Finkbeiner, D. P. 2011, *ApJ*, 737, 103
 Schneider, S. E., Thuan, T. X., Magri, C., & Wadiak, J. E. 1990, *ApJS*, 72, 245
 Science Software Branch at STScI. 2012, *PyRAF: Python alternative for IRAF*, Astrophysics Source Code Library, record ascl:1207.011
 Shivvers, I., Filippenko, A. V., Silverman, J. M., et al. 2019, *MNRAS*, 482, 1545

¹⁸ <https://wiserep.weizmann.ac.il/>

Telescope/Instrument	Bands	Filter System	Reference System	Calibration Source
P48/ZTF	<i>gri</i>	ZTF	AB	PS1/Internal
Swift/UVOT	UBV M2 W1 W2	Custom	Vega	Internal
MPG 2.2m/GROND	<i>g'r'i'z'</i>	Sloan/Custom	AB	SDSS DR12
MPG 2.2m/GROND	<i>JHK_s</i>	Johnson/Custom	Vega	2MASS All-Sky DR
P60/SEDM-RC	<i>ugri</i>	Sloan/Astrodon	AB	SDSS/PS1
NOT/ALFOSC	<i>gri</i>	Sloan	AB	PS1

Table 11. Overview of facilities used for photometric followup observations as well as their respective native filter systems and calibration sources.

Skilling, J. 2004, in American Institute of Physics Conference Series, Vol. 735, Bayesian Inference and Maximum Entropy Methods in Science and Engineering: 24th International Workshop on Bayesian Inference and Maximum Entropy Methods in Science and Engineering, ed. R. Fischer, R. Preuss, & U. V. Toussaint, 395–405

Skilling, J. 2006, Bayesian Analysis, 1, 833

Skrutskie, M. F., Cutri, R. M., Stiening, R., et al. 2006, AJ, 131, 1163

Smartt, S. J., Valenti, S., Fraser, M., et al. 2015, A&A, 579, A40

Soderberg, A. M., Berger, E., Page, K. L., et al. 2008, Nature, 453, 469

Soffitta, P., Feroci, M., Piro, L., et al. 1998, IAU Circ., 6884, 1

Speagle, J. S. 2020, MNRAS, 493, 3132

Stritzinger, M., Hamuy, M., Suntzeff, N. B., et al. 2002, AJ, 124, 2100

Stritzinger, M. D., Taddia, F., Burns, C. R., et al. 2018, A&A, 609, A135

Taddia, F., Sollerman, J., Fremling, C., et al. 2019, A&A, 621, A71

Taddia, F., Sollerman, J., Leloudas, G., et al. 2015, A&A, 574, A60

Taddia, F., Stritzinger, M. D., Bersten, M., et al. 2018, A&A, 609, A136

Takada-Hidai, M., Aoki, W., & Zhao, G. 2002, PASJ, 54, 899

Tartaglia, L., Fraser, M., Sand, D. J., et al. 2017, ApJ, 836, L12

Tauris, T. M., Langer, N., & Podsiadlowski, P. 2015, MNRAS, 451, 2123

Tody, D. 1993, in Astronomical Society of the Pacific Conference Series, Vol. 52, Astronomical Data Analysis Software and Systems II, ed. R. J. Hanisch, R. J. V. Brissenden, & J. Barnes, 173

Virtanen, P., Gommers, R., Oliphant, T. E., et al. 2020, Nature Methods, 17, 261

Williamson, M., Modjaz, M., & Bianco, F. B. 2019, ApJ, 880, L22

Woolley, S. E., Langer, N., & Weaver, T. A. 1993, ApJ, 411, 823

Wygoda, N., Elbaz, Y., & Katz, B. 2019, MNRAS, 484, 3941

Yamanaka, M., Nakaoka, T., Tanaka, M., et al. 2017, ApJ, 837, 1

Yaron, O. & Gal-Yam, A. 2012, PASP, 124, 668

Yoon, S.-C., Chun, W., Tolstov, A., Blinnikov, S., & Dessart, L. 2019, ApJ, 872,

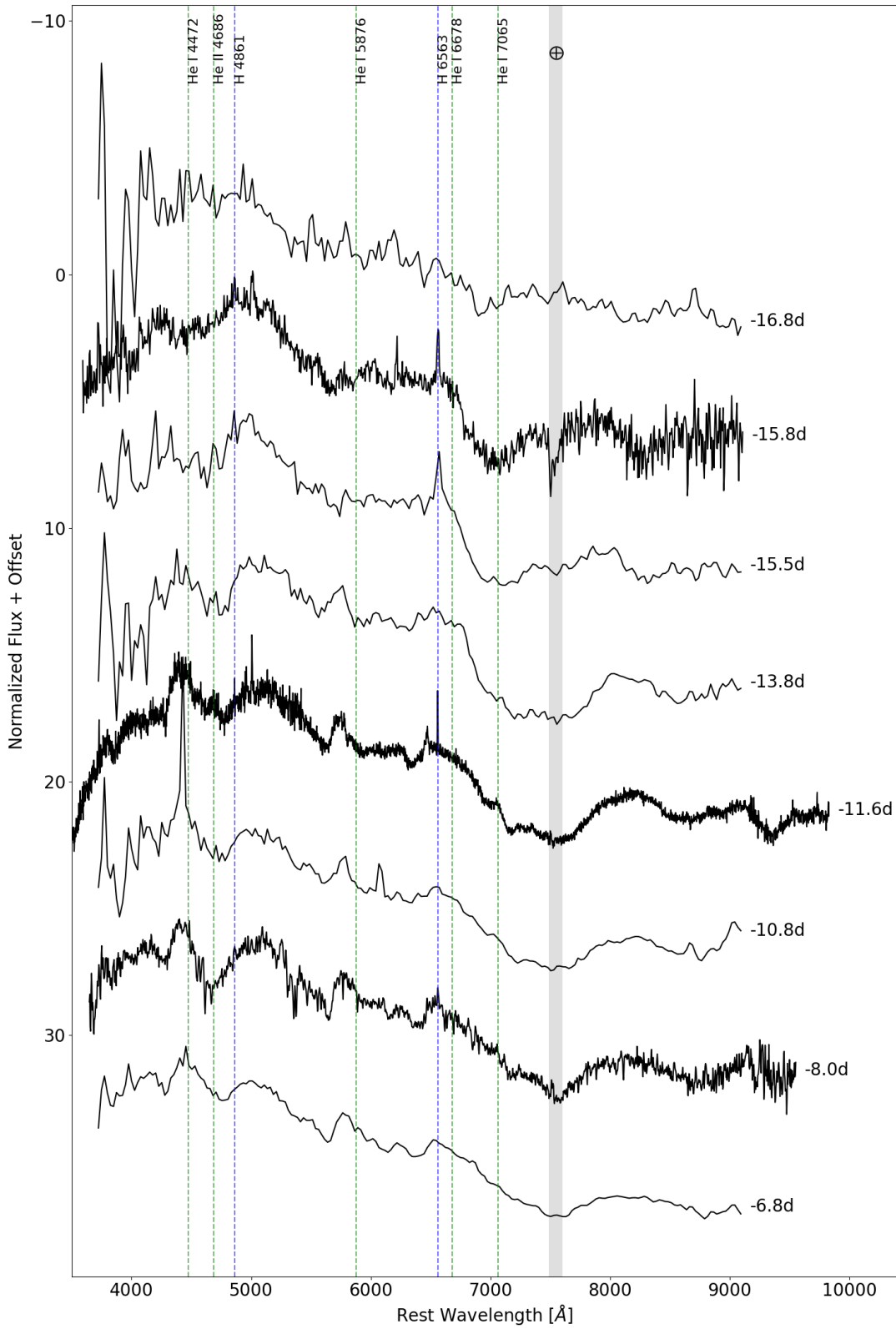


Fig. 10. Spectral sequence of obtained spectra from discovery to before peak. The observation phase of each spectrum is denoted on the right of each spectrum. Rest wavelengths of strong He I features have been marked in green, and the position of Balmer lines are denoted in blue. A Telluric absorption feature has been denoted with a shaded region and a \oplus symbol.

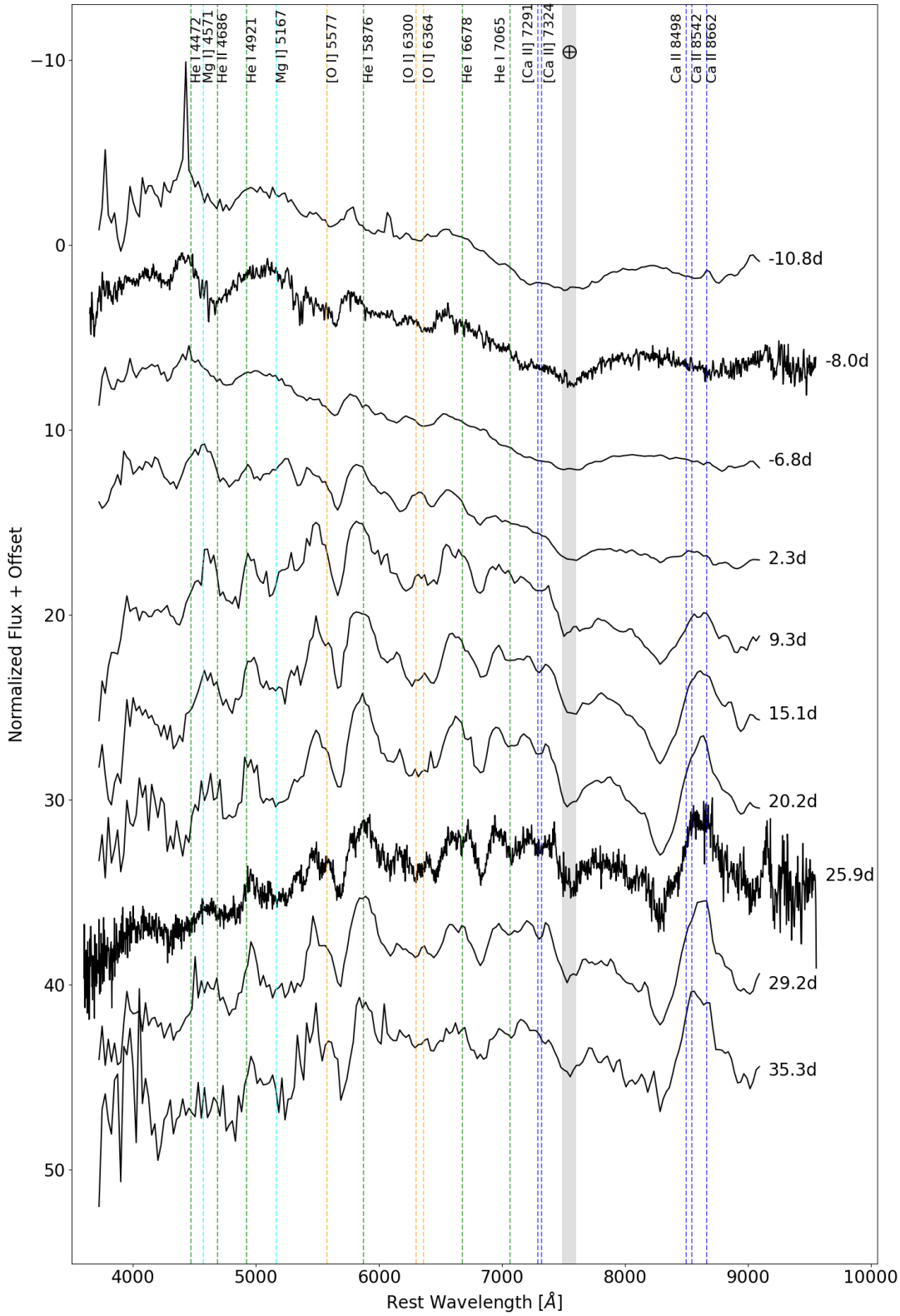


Fig. 11. Spectral sequence of obtained spectra around the photospheric phase. The notation is the same as in Fig. 10, but here we have also marked the wavelengths of several intermediate mass elements.

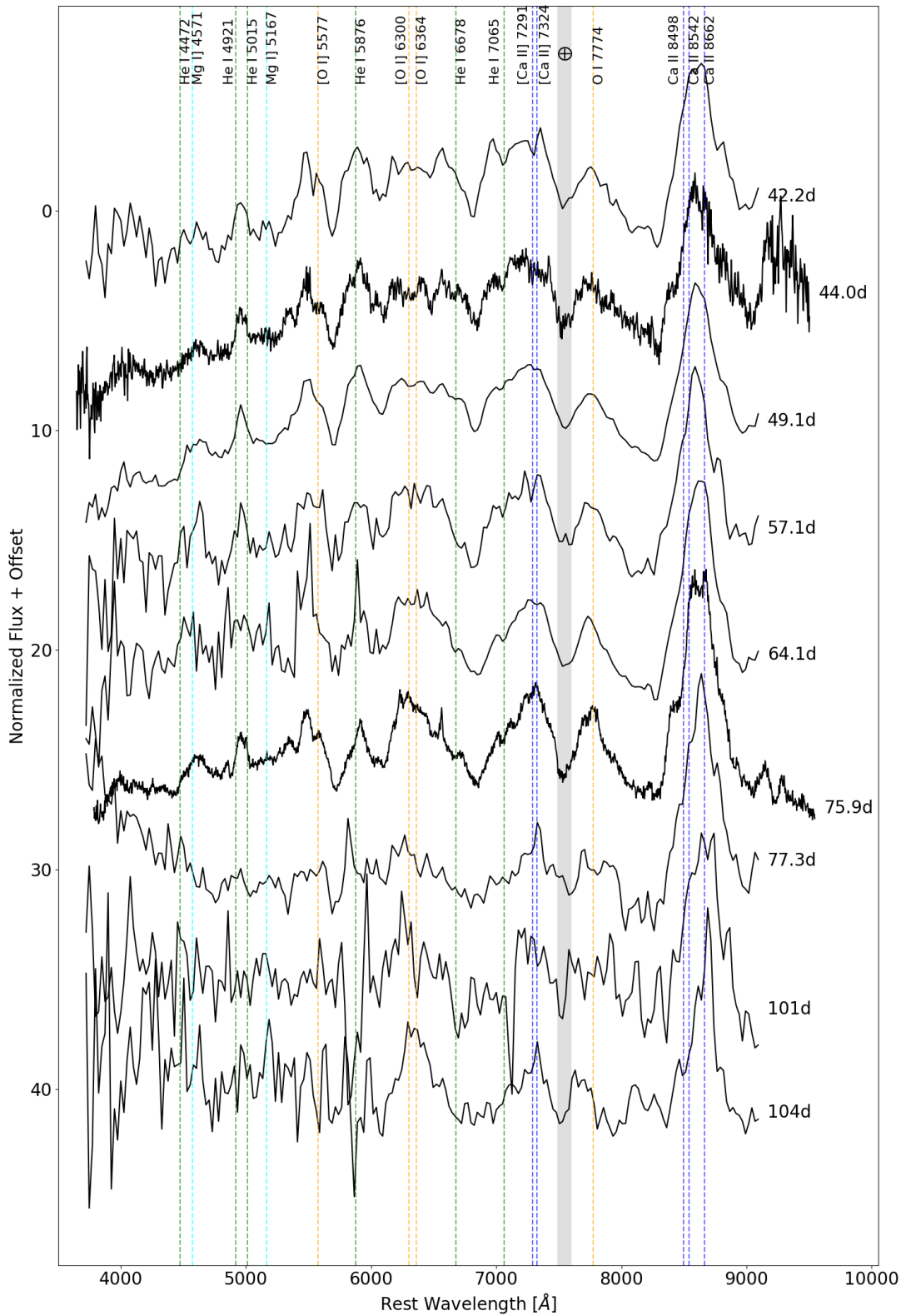


Fig. 12. Spectral sequence of obtained spectra in the pre-nebular phase. The notation is the same as in Fig. 10, but here we have also marked the wavelengths of several intermediate mass elements.

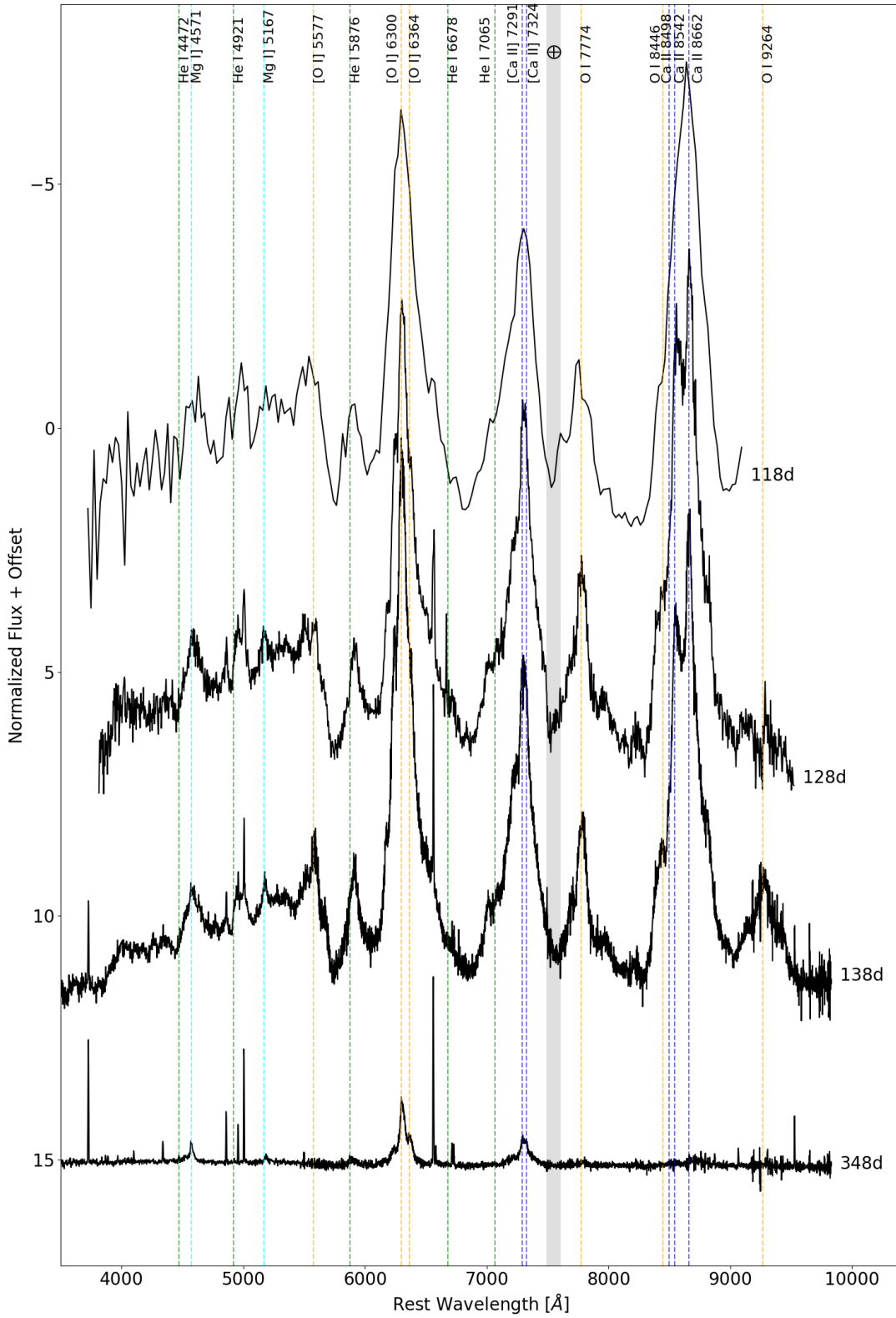


Fig. 13. Spectral sequence of SN 2019odp in the nebular phase. We have marked several of the O I lines as well as some Ca II lines.

Appendix A: Photometric Models

Transient	Band	Model
SN 2019odp	ugri	plateau-contardo
SN 2019odp	zJHK	linear
iPTF13bvn	Ugriz	plateau-contardo
SN 2008D	UBVri	prebump-contardo
SN 1998bw	UBV R _C I _C	plateau-conardo
SN 2002ap	UBVRI	plateau-contardo

Table A.1. Used photometric models per supernova and band

In this section we describe the used analytic photometry light curve models and priors for the models. We use different models depending on the lightcurve coverage and the shape of the early excess (if there was one detected) with the decision being specific to the photometric band. The assignment of photometric model to a given transient and band is listed in Table A.1. All analytic functions use the phase relative to the prior peak estimate: $\Delta t \equiv t - t_{\text{peak}}$.

Our (complex) lightcurve models are based on the lightcurve model by Contardo et al. (2000) (hereafter C20):

$$m_{\text{C20}}(\Delta t) = \delta(\Delta t) \left(\alpha + \beta \Delta t + A_{\text{DF}} \exp \frac{-(\Delta t - t_{0,\text{DF}})}{2\sigma_{\text{DF}}^2} \right), \quad (\text{A.1})$$

where Δt is the phase relative to the main peak prior time, $\delta(t)$ is the explosion scaling function, α is the linear intercept, β is the linear slope, A_{DF} is the amplitude of the main diffusion peak gaussian, $t_{0,\text{DF}}$ is the phase offset of the main diffusion peak gaussian and σ_{DF} is the width of the gaussian. The rise scaling function is given as:

$$\delta(\Delta t)^{-1} = 1 - \exp \frac{-(\Delta t - t_{0,\text{rise}})}{\tau_{\text{rise}}}, \quad (\text{A.2})$$

where $t_{0,\text{rise}}$ is the phase offset of the rise scaling function, τ_{rise} is the rise timescale.

We derive two modified lightcurve models from the C20 depending on the shape of the early excess:

1. The ‘‘plateau-contardo’’ model adds a smoothing function $g(t)$ to interpolate between the plateau magnitude m_{plat} and the m_{C20} function:

$$g(\Delta t) = \left(\arctan \left(\frac{\Delta t - t_{0,\text{plat}}}{\tau_{\text{smooth}}} \right) \frac{1}{\pi} + 0.5 \right)^2 \quad (\text{A.3})$$

$$m_{\text{PLC}}(\Delta t) = m_{\text{plat}} + (m_{\text{C20}}(\Delta t) - m_{\text{plat}})g(\Delta t) \quad (\text{A.4})$$

This introduces three additional parameters to the C20 model that we allow to vary in a reasonable range: plateau magnitude m_{plat} , plateau end time $t_{0,\text{plat}}$ and the smoothing timescale τ_{smooth} .

2. The ‘‘prebump-contardo’’ model adds a secondary gaussian peak at a peak relative to the main peak:

$$m_{\text{PBC}}(\Delta t) = p_{\text{C20}} + \delta(t)A_{\text{PB}} \exp \frac{-(\Delta t - t_{0,\text{PB}})}{2\sigma_{\text{PB}}^2} \quad (\text{A.5})$$

This introduces three additional parameters to the model: pre-bump amplitude A_{PB} , pre-bump width σ_{PB} and center time of the pre-bump $t_{0,\text{PB}}$.

If the data only covers a small time range before/after peak we use a linear model instead:

$$m_{\text{lin}}(\Delta t) = \alpha + \frac{\beta}{1000} \Delta t \quad (\text{A.6})$$

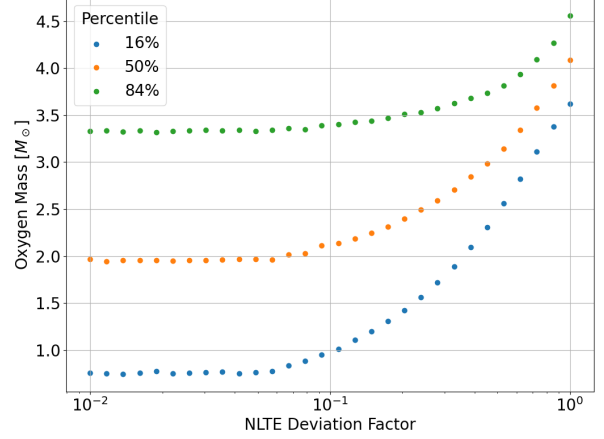


Fig. B.1. Plot showing the oxygen mass percentiles as a function of the minimum LTE departure coefficient d_2 .

Appendix B: Oxygen Mass Modelling

Appendix B.1: NLTE Deviation Factor

The LTE departure coefficient is defined as follows:

$$d_2 = \frac{n_2}{n_2^{\text{LTE}}} \quad (\text{B.1})$$

We estimate the sensitivity to deviations from LTE conditions by running the fitting procedure for a spectrum multiple times in a sequence where we vary the allowed maximum LTE departure coefficient d_2 from 0.01 to 1.0 (where 1.0 means LTE conditions). The resulting change due to the change of the LTE departure can be seen in Fig. B.1.

We get a rough estimate for the LTE departure coefficient d_2 by estimating the electron density n_e from the O I $\lambda 7774$ recombination line and using the following relation:

$$d_2 \approx \left(1 + 1.44 \left(\frac{T}{1000 \text{ K}} \right)^{-0.034} \left(\frac{n_e}{10^8 \text{ cm}^{-3}} \right)^{-1} \right)^{-1} \quad (\text{B.2})$$

which we got by dividing eqn. 2 from Houck & Fransson (1996) by eqn. 2 from Jerkstrand et al. (2015). To approximate the electron density we use the oxygen recombination lines that are visible in the earlier spectra. We can use the following relation from Jerkstrand et al. (2015) to relate the line luminosity to the electron density (their eqn. 3):

$$L_{\text{rec}} = \frac{4\pi}{3} (V_{\text{core}} t)^3 \Psi \alpha_{\text{eff}} f_O n_e^2 h\nu, \quad (\text{B.3})$$

where V_{core} is the line width, t is the time since explosion, Ψ is the fraction of electrons provided by oxygen ionizations and f_O is the oxygen zone filling factor.

We assume Ψ to be of order unity (from Jerkstrand et al. (2015)). We estimate V_{core} from the measured gaussian line width. Since α_{eff} depends on the temperature, we use the values from Jerkstrand et al. (2015, their sect. C.1) for three different temperatures. Using $\alpha(T = 2500) = 2.8 \times 10^{-13}$, $\alpha(T = 5000) = 1.6 \times 10^{-13}$ and $\alpha(T = 7500) = 1.1 \times 10^{-13}$ and a crudely estimated line luminosity of $L \approx 27 \cdot 10^{38} \text{ erg s}^{-1}$ and as well as the line width estimated velocity of 2464 km s^{-1} (both from the +158 d Keck spectrum) we estimate $n_e \sqrt{f_O}$ to be: $2.2 \cdot 10^8 \text{ cm}^{-3}$

(2500 K), $2.9 \cdot 10^8 \text{ cm}^{-3}$ (5000 K) and $3.5 \cdot 10^8 \text{ cm}^{-3}$ (7500 K). This is in line to the values seen in [Jerkstrand et al. \(2015\)](#). Using [Equation B.2](#) we get a range of 0.6 to 0.72 for LTE departure coefficient d_2 for an assumed zone filling factor of one. Higher filling factors would yield even higher values. However the re-combination lines can be emitted from higher density regions than the nebular lines we are using in the main analysis and are thus not really suitable for quantitative analysis and we thus do not use the derived d_2 value/range.

Appendix B.2: Spectral Fitting Results

In this section we show the best fit results from the spectral line profile models. In [Fig. B.2](#), [Fig. B.3](#) and [Fig. B.4](#) we show the relevant spectral fitting regions with model spectra drawn from the posterior distribution overplotted. The corresponding corner plots visualizing the posterior distributions can be found in [Fig. B.5](#), [Fig. B.6](#), [Fig. B.7](#).

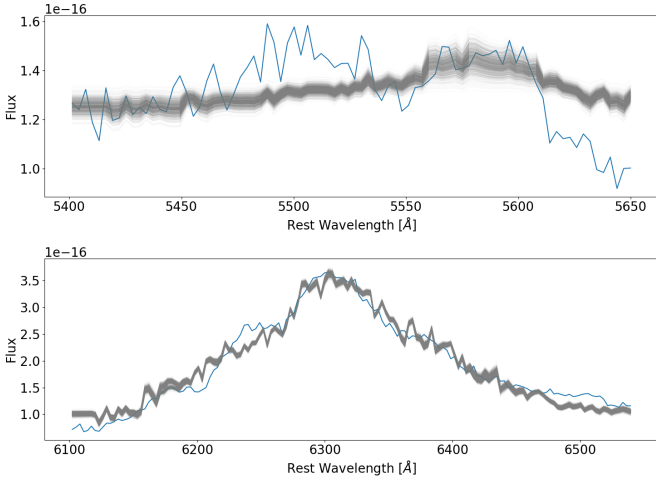


Fig. B.2. NOT/ALFOSC spectrum at 128 days post-peak with model spectra drawn from the posterior distribution of the model overlaid in grey.

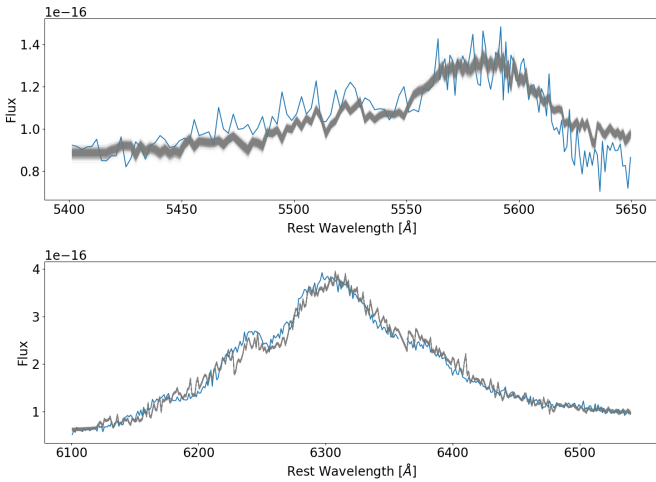


Fig. B.3. Early Keck/LRIS spectrum at 138 days post-peak with model spectra drawn from the posterior distribution of the model overlaid in grey.

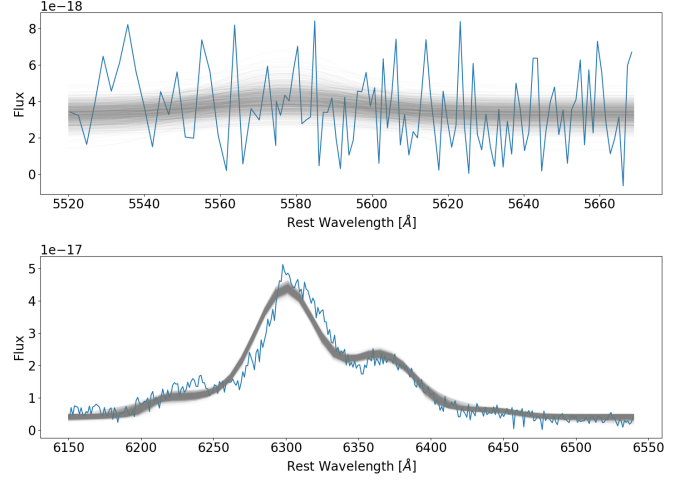


Fig. B.4. Late Keck/LRIS spectrum at 358 days post-peak with model spectra drawn from the posterior distribution of the model overlaid in grey.

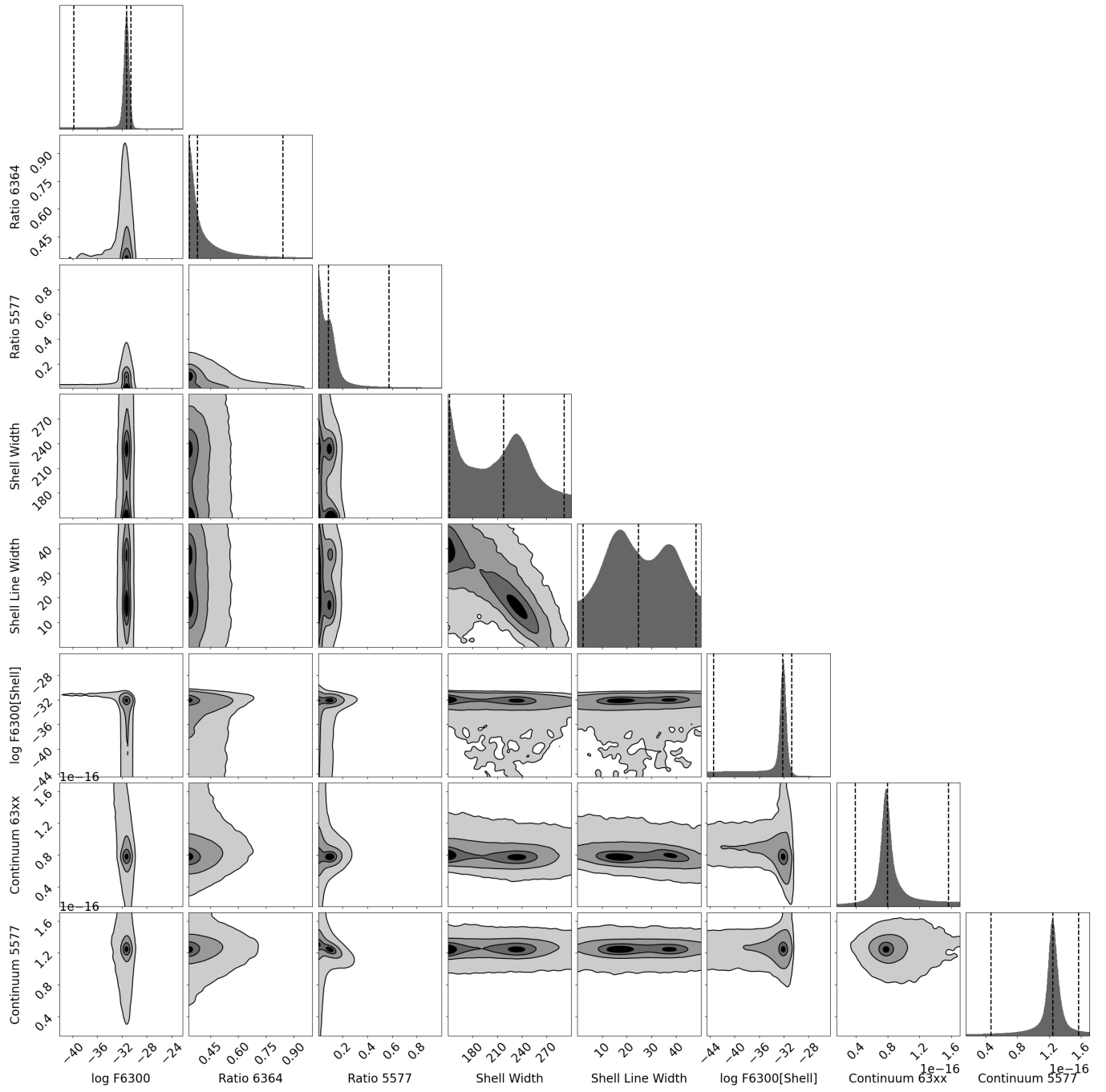


Fig. B.5. Corner plot of the O I λ 7774 spectral line profile model for the NOT/ALFOSC spectrum at 128 days post-peak.

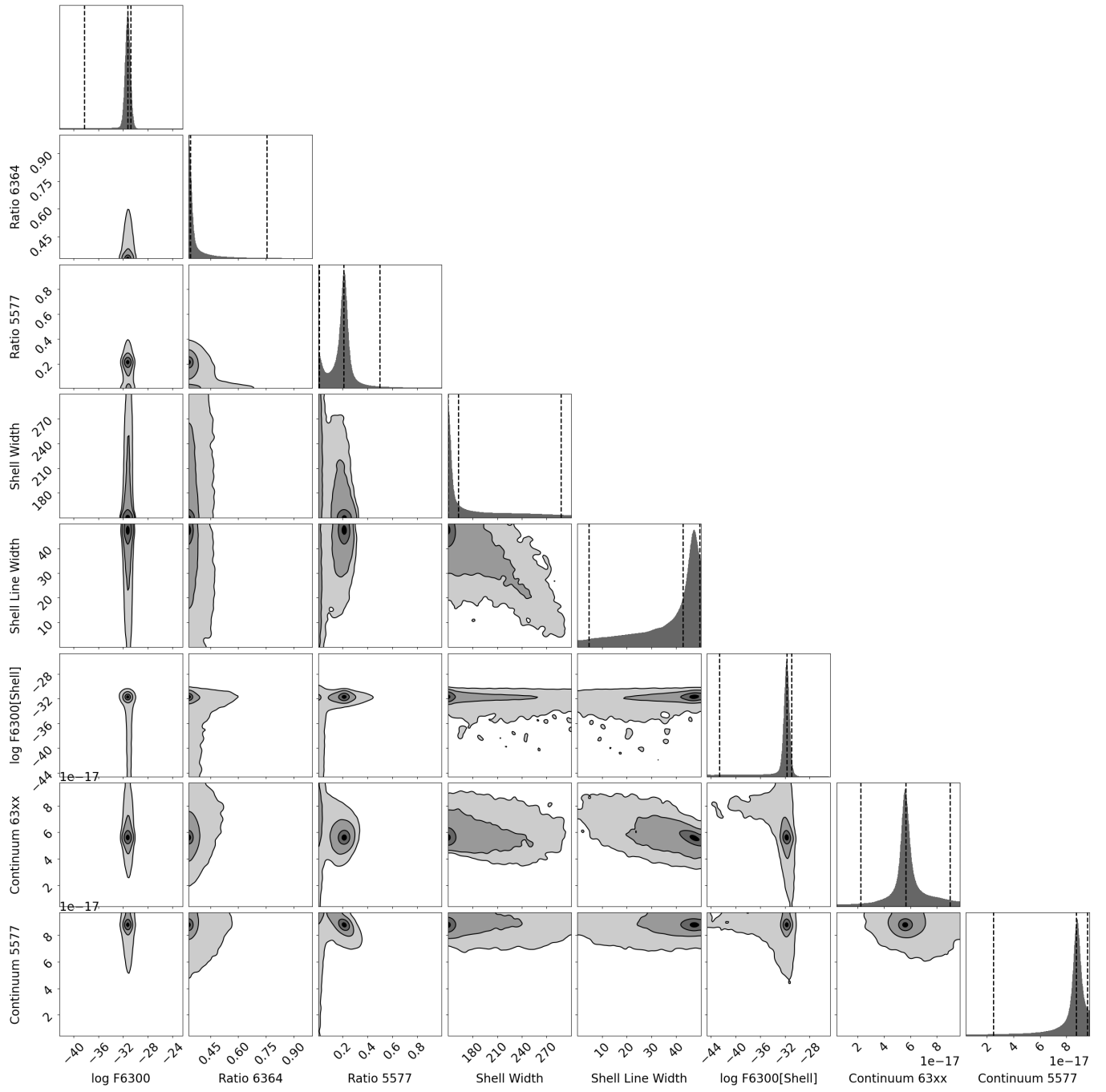


Fig. B.6. Corner plot of the $O\text{I } \lambda 7774$ spectral line profile model for the early Keck/LRIS spectrum at 138 days post-peak.

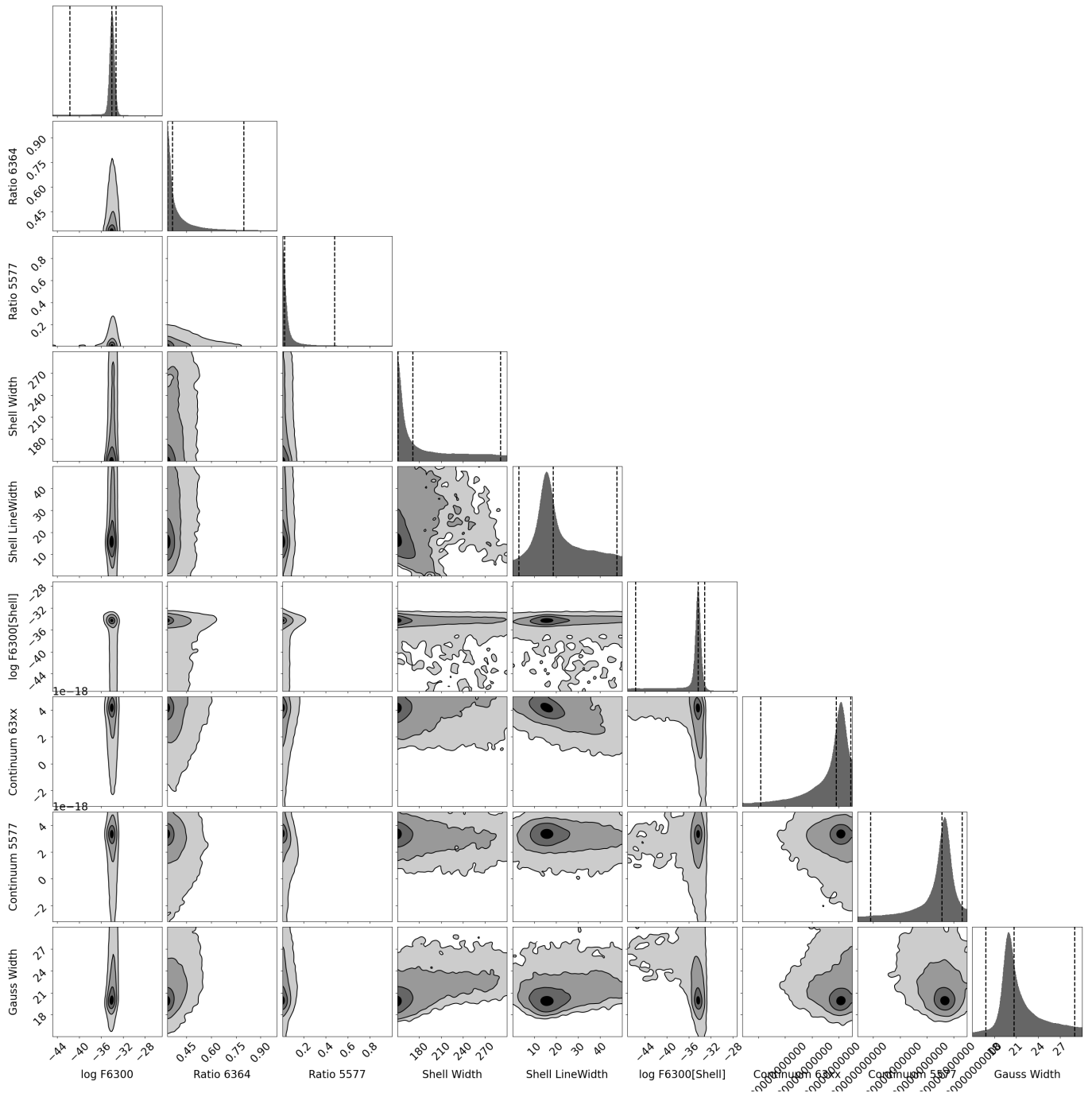


Fig. B.7. Corner plot of the gaussian spectral line profile model for the late Keck/LRIS spectrum at 358 days post-peak.

Appendix B.3: Physical Fitting Results

The resulting corner plots of the fits of the second stage of the fitting routine (outlined in Sect. 4.3.2) are shown in Fig. B.8, Fig. B.9, Fig. B.10. The used input line fluxes (converted to luminosities) are given in Table 10.

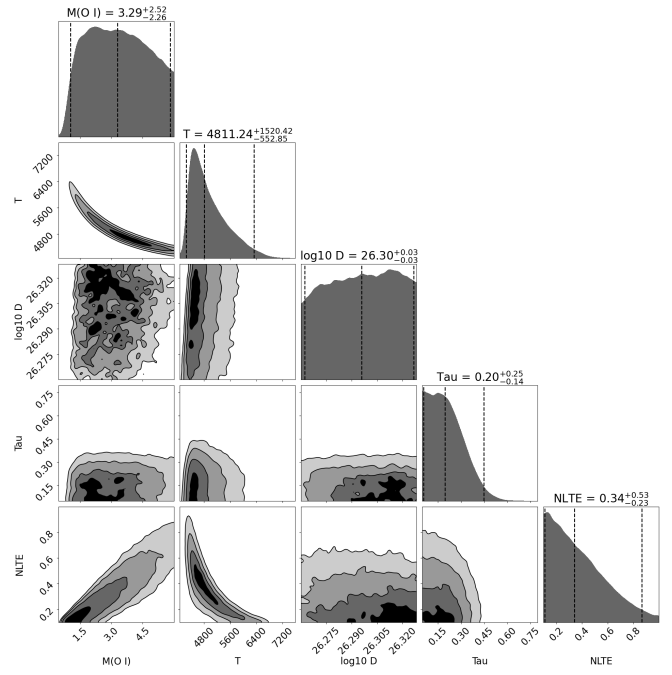


Fig. B.8. Corner plot of the physical oxygen model for the NOT/ALFOSC spectrum at 128 days post-peak.

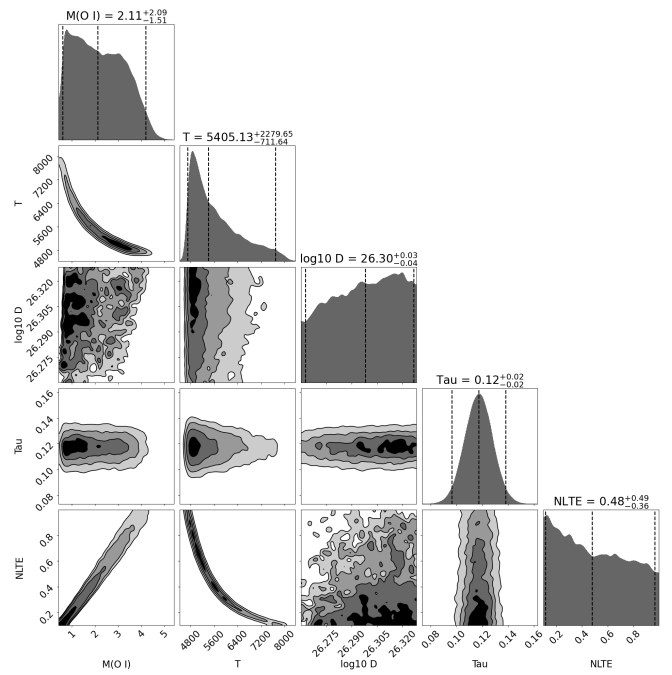


Fig. B.9. Corner plot of the physical oxygen model for the early Keck/LRIS spectrum at 138 days post-peak.

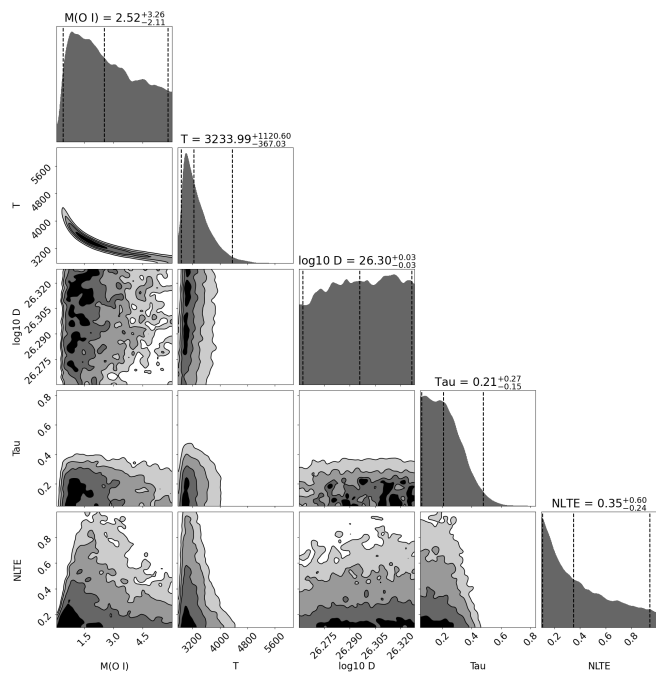


Fig. B.10. Corner plot of the physical oxygen model for the late Keck/LRIS spectrum at 358 days post-peak.

Appendix C: Photometric Blackbody Fitting

We use the interpolated and pre-processed lightcurve constructed by the method described in Sect. 2.3. We construct the time grid to perform the fitting by selecting all observations between the first time all selected filter bands had at least one detection and the peak and then selecting all days post-peak that had at least one observation. This ensures we are only interpolating the lightcurve and never have to rely on extrapolating it (which is highly uncertain at the very early epochs).

For each time on the time grid we estimate the extinction-corrected magnitude in all filter bands. Next we fit a three-parameter Bayesian model to these observations: temperature $\log T$, radius $\log R$ and the distance D . We follow the suggestion by Arcavi (2022) and use a log-uniform prior for the temperature (although we use nested sampling instead of MCMC). The distance is a nuisance parameter, which is constrained by the redshift uncertainty. In the likelihood function we generate a blackbody SED using the temperature and radius. We then perform synthetic photometry using the corresponding filter curves to compare to the lightcurve. We perform the posterior calculation using the nested sampling code *dynesty*.

Appendix C.1: Validation

We compare the resulting temperature and radius between three different filter combinations: *gri*, *ri* and *rizJH*. The comparison is shown in Fig. C.1. We only have a full spectral coverage from optical to NIR between 40 and 80 days.

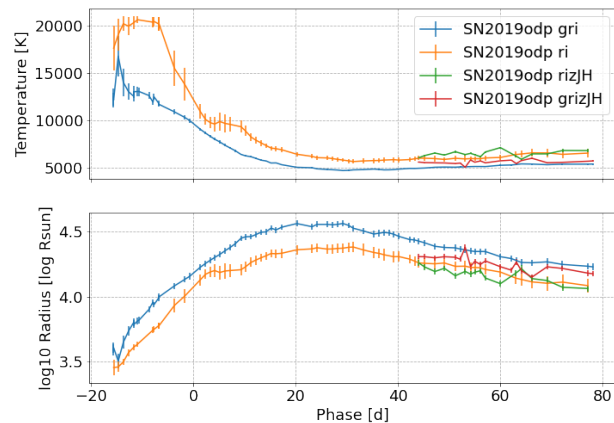


Fig. C.1. Comparison between three filter sets.